論文 / 著書情報
Article / Book Information

題目(和文)	二層非圧縮流体からなる天体が自転している場合の重力平衡形状とその安定性 : 月分裂仮説との関係
Title(English)	Equilibrium figure and stability of rotating, self-gravitating body composed of two-layered incompressible fluids : implication to the fission hypothesis of the lunar origin
著者(和文)	久保岡俊宏
Author(English)	Toshihiro Kubo-oka
出典(和文)	学位:博士(理学), 学位授与機関:東京工業大学, 報告番号:甲第3127号, 授与年月日:1996年3月26日, 学位の種別:課程博士, 審査員:
Citation(English)	Degree:Doctor (Science), Conferring organization: Tokyo Institute of Technology, Report number:甲第3127号, Conferred date:1996/3/26, Degree Type:Course doctor, Examiner:
学位種別(和文)	博士論文
Type(English)	Doctoral Thesis

Equilibrium Figure and Stability of Rotating, Self-Gravitating Body Composed of Two-Layered Incompressible Fluids

- Implication to the Fission Hypothesis of the Lunar Origin -

Toshihiro Kubo-oka

Department of Applied Physics
Tokyo Institute of Technology

Doctoral Thesis
January 1996

Abstracts

The geochemical research on the bulk composition of the Moon infers that the lunar material comes from the terrestrial magma ocean. The giant impact is disqualified for the mechanism to strip the magma ocean since the results of the numerical simulations of the giant impact are inconsistent with the chemical composition of the Moon. Thus, the classical rotational fission hypothesis seems to be a more favorable candidate of the stripping mechanism although it has several physical difficulties.

In most of the previous studies on the rotational fission, the proto-Earth was treated as a single-layered body composed of an incompressible fluid. However, as a result of the core formation, the proto-Earth is no longer homogeneous. Thus, the effect of inhomogeneity of the proto-Earth must be taken into account. We regard the proto-Earth as a superposition of the two layers of incompressible fluids with different densities ρ_0 and $\rho_1 = \rho_0 + \delta\rho$. The most important parameters in our calculations are the ratio of the volume of the core to the volume of the proto-Earth V_1/V_0 and the density ratio $\delta\rho/\rho_0$.

We first look for the gravitational equilibrium figure of such rotating two-layered axisymmetric masses numerically. When the rotation is slow, *i.e.*, the coaspect ratio $\epsilon = \sqrt{1 - a_3^2/a_1^2}$ (a_1 and a_3 denote the semiaxe of the body surface) is small, both the body surface and the core-mantle boundary are well approximated by spheroids. As the body rotates faster, the body surface begins to deviate from a spheroid while the core-mantle boundary is kept to be spheroidal. We find that the coaspect ratio has a critical value ϵ_c. If the coaspect ratio beyonds this critical value, the outward centrifugal force overcomes with the inward gravitational force and the body can no longer keep a single figure.

We next investigate extensively the stability of the equilibrium figures obtained numerically against the small perturbations using the criterion derived by Chandrasekhar and Lebovitz (1962). For the cases where the values of the parameters $\delta\rho/\rho_0$ and V_1/V_0 are suitable for the proto-Earth, the condition of the secular instability is almost the same as that for the

Maclaurin spheroid, *i.e.*, the homogeneous spheroid. Moreover, the body reaches the critical coaspect ratio before the dynamical instability occurs and mass shedding from the equator is expected to begin. However, the angular momentum that corresponds to the critical coaspect ratio is almost the same as that needed to trigger the dynamical instability.

Therefore, the condition of the rotational fission is not eased by the inhomogeneity of the proto-Earth. We should exclude the rotational fission hypothesis from the candidates of the mechanism to strip the materials from the terrestrial magma ocean since it seems to be impossible to gain enough angular momentum.

Contents

1. Introduction

The problem of the lunar origin has been a "Gordian Knot" for hundreds of years. Since the 17th century, the era of Newton, hundreds of scientist attacked this problem and proposed tens of hypothesises and their variations for the lunar origin. However, we have not got a "sword" to cut the knot, in other words, we have not established the theory which satisfies both the dynamical and the geochemical conditions. Let us first review briefly both the dynamical and the geochemical constraints that the theory of the lunar origin must satisfy.

1.1. Dynamical constraints on the theory of the lunar origin

(1) Angular momentum of the Earth-Moon system

It is generally accepted that the Earth was formed through the accumulation of planetesimals. The angular momentum of the present Earth-Moon system, which is the sum of the rotational angular momentum of the Earth and the orbital angular momentum of the Moon, is extraordinary large and it had been believed that the angular momentum of the Earth-Moon system could not be explained by the collision of the planetesimals (e.g., Giuli, 1968). At the same time, this is one of the crucial disadvantages against the fission origin of the Moon.

Estimation of the angular momentum induced by the accumulation is based on the assumption that the spatial distributions of the planetesimals is uniform. The rotational angular momentum which the proto-Earth gains through accretion of uniformly distributed planetesimals is almost canceled out and the resultant angular momentum is very small. But, the collisions between the protoplanet and the planetesimals which distribute nonuniformly bring the large amount of angular momentum in the same direction of rotation (Ida and Nakazawa, 1990; Lissauer and Kary, 1991). In fact, recent N-body calculations of the planetesimals around the Sun reveal that, as the gravitational scattering due to the protoplanet takes effect, the spatial distribution of the planetesimals around the protoplanet becomes nonuniform (Ida and Makino, 1993; Tanaka and Ida, 1995). The angular momentum of the present Earth-Moon system may be explained by this scenario (Ohtsuki and Ida, 1995). Hence, the fission theory of the Moon is not in conflict with the scenario of the planetary growth.

(2) Constraint on the 'birthplace' of the Moon

The studies on the tidal orbital evolution of the Moon (see, *e.g.*, Burns, 1986) show that the Moon gradually moves away from the Earth. In Fig. 1.1, we show the behavior of the lunar orbital evolution in the $(a,\ e)$-plane, where a and e denote the semimajor axis and the eccentricity of the lunar orbit, respectively (Mignard, 1982). The curves are distinguished by the parameter A, which is the ratio of the amount of the energy dissipation within the Moon to that within the Earth. If we go back the evolutional path in time, we can know where the Moon was located 4.6 billions years ago. However, lack of our precise knowledge on the amount of energy dissipation within the Earth and the Moon prevents us from knowing the precise rate on how fast the tide affects the semimajor axis of the Moon. Therefore, the exact birthplace of the Moon is unknown. Nevertheless, it is certain from the theory of the tidal evolution of the Moon that the distance between the Earth and the Moon had been always larger than the co-rotation radius R_c which is given by

$$R_c \sim 2.35 R_{\rm E} \quad , \tag{1.1}$$

where $R_{\rm E}$ is the radius of the Earth (note that R_c does not depend on the dissipation ratio A). If the Moon was located at a distance less than $R_c$from the Earth, then the Moon must have fallen onto the Earth. Therefore, we can safely say that the 'birth place' of the Moon was more distant from this limiting radius.

(3) Inclination of the lunar orbit

At present, the orbital plane of the Moon and the equatorial plane of the Earth are not identical. The inclination i is about 5.1 degree. Not only the semimajor axis and the eccentricity of the lunar orbit, the inclination also gradually varies in time by the tidal interaction among the Earth, the Moon, and the Sun (Mignard, 1982). In Fig. 1.2, we show the evolutionary path

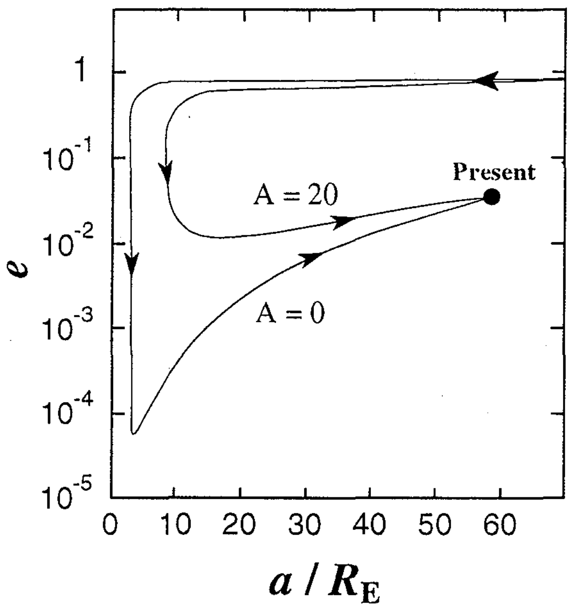

Fig. 1.1. The behavior of the lunar orbital evolution due to tide (from Mignard, 1982). In this figure, a and e are the semimajor axis and the eccentricity of the lunar orbit, respectively. The semimajor axis is normalized by the radius of the Earth, R_E. Arrows are pointing to the future and the solid circle indicates the present state of the Moon. The curves are distinguished by the parameter A, which is the ratio of the dissipated energy within the Moon to that within the Earth.

in the (a, I)-plane where I is the angle between the spin vector of the Earth and the vector normal to the lunar orbital plane. From this figure, we can see that I has never been equal to zero. Although this has been considered to be a disadvantage against the fission theory of the Moon, we can avoid the difficulty considering either of the orbital plane of the Moon or the equatorial plane had to be tilted after the Moon was formed in the equatorial plane of the Earth.

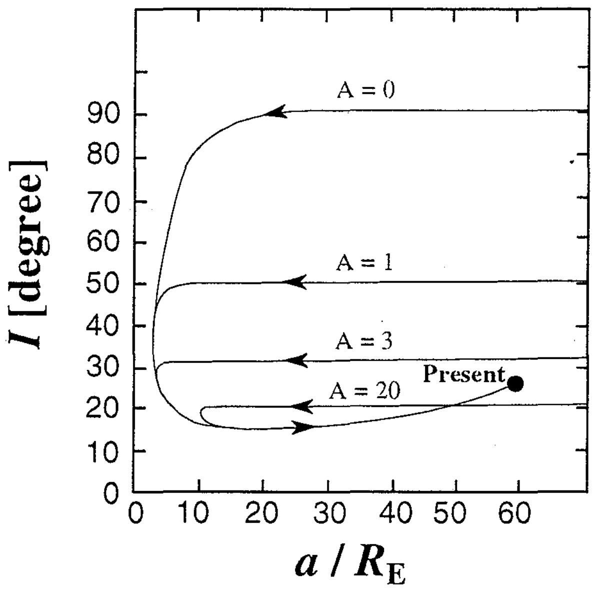

Fig. 1.2. The behavior of the lunar orbital evolution in the (a, I)-plane (from Mignard, 1982) where I denotes the angle between the spin vector of the Earth and the vector normal to the lunar orbital plane. Arrows are pointing to the future and the solid circle indicates the present state of the Moon. Furthermore, a, R_E, and A have the same meanings as in Fig. 1.1.

(4) The size of the lunar core

The moment of inertia of the Moon I_M is estimated to be

$$I_M = 0.3905 M_M R_M^2 \quad , \tag{1.2}$$

where M_M and R_M are the mass and radius of the Moon, respectively (Ferrari et al., 1980). This value is almost the same as that of the homogeneous sphere and infers that the internal structure of the Moon is almost homogeneous. Namely, even if there exists the metallic core inside the Moon, its radius must be small up to 460 km and its mass is at most 6 percent of the lunar mass (Hood and Jones, 1985). This gives a strong constraint on the formation process of the Moon.

1.2. Geochemical constraints

(1) Volatile elements

In general, the Moon surface and the terrestrial mantle are substantially depleted in volatile elements such as K, Rb, and Cs compared with those of CI chondrite (see, *e.g.*, Ringwood, 1979; Taylor, 1986). For example, the terrestrial Rb/Sr ratio is 0.031 and the lunar Rb/Sr ratio is 0.009. They are much smaller than the CI value of 0.30. It is natural to consider that the Moon and the Earth were strongly heated during or just after their formation. It is also important to note that the abundance of volatile elements in the Moon is clearly more depleted compared to the Earth's mantle.

(2) Iron

The mean density of the Moon ($\bar{\rho} = 3.34$ g/cm^3) is lower than that of the terrestrial materials at zero pressure ($\bar{\rho} = 4.45$ g/cm^3) and is almost equal to the mean density of the terrestrial upper mantle ($\bar{\rho} = 3.30$ - 3.40 g/cm^3). It may be inferred that the Moon has smaller proportion of heavy elements than the Earth. The only element which can explain this feature is Fe and it is generally accepted that the Moon is depleted in Fe compared to the Earth and other terrestrial-type planets.

(3) Chromium, Vanadium, and Manganese

Elements like Cr, Mn, and V show siderophile behavior at high pressure. The abundance of these elements in the Moon are similar to that in the terrestrial mantle and they are depleted by the factors of 0.6-0.2 in the mantles of both bodies compared to those of CI chondrites. Ringwood (1989) suggested that V, Mn, and Cr were absorbed into the terrestrial core during the core formation process. Moreover, Kato and Ringwood (1989) showed that the depletion of these elements does not occur in martian-size objects or smaller bodies. So, this feature suggests that the materials of the Moon came from a Venus-sized object or a larger body.

(4) Siderophile trace elements

The abundances of the siderophile elements can be divided into two groups. The concentrations of Ni, Co, and W in the upper mantles of the Moon and the Earth are similar with each other, while Ge, Sb, and Re in the upper mantle of the Moon is strongly depleted compared to the upper mantle of the Earth (Ringwood 1979; Rammensee and Wänke, 1977). Ringwood and Kesson (1977) argued that the elements which belong to the second group are relatively volatile, and were lost from the Moon during its formation. If it were true, the resemblance of the abundance of the first group suggests that the lunar materials come from the terrestrial mantle.

(5) Oxygen isotopes

The oxygen isotopic composition of the lunar and the terrestrial basalts show the same pattern (Clayton et al., 1976). This implies that the lunar materials may have come from the Earth, or at least, may have formed in the vicinity of the Earth in the solar nebula.

(6) The mg$^\sharp$ number

The (MgO/MgO+FeO) ratio called the mg$^\sharp$ number is an important index to assign the chemical composition of rocky materials. The mg$^\sharp$ number of the bulk Moon is estimated to be $0.77 \sim 0.85$, while the mg$^\sharp$ number of the terrestrial upper mantle is estimated to be 0.89 (see, *e.g.*, Drake, 1986). The mg$^\sharp$ number of Mars is almost the same with the value of the Moon. However, according to a resent study about the chemical composition of the magma ocean (Okuchi, 1995), the mg$^\sharp$ number of the Moon is identical to that of the terrestrial magma ocean which is formed at a depth of about 300 km with a temperature as high as 1600 °C. Furthermore, the abundance of the siderophile elements like Ni, Co, and W of the Moon agrees with those estimated from this model of the magma ocean. These support strongly that the lunar materials were supplied from the terrestrial mantle.

As we have seen above, from the geochemical point of views (1) to (6), it is natural to consider the materials from which the Moon was formed came from the deep magma ocean of the proto-Earth.

1.3. Hypothesises of the lunar origin

Many hypothesises have been proposed on the lunar origin until now. We will summarize them briefly.

(1) Giant impact hypothesis

Hartmann and Davis (1975) first suggested a possibility that a planet-sized object collides with the proto-Earth and the Moon was formed from the ejected debris. Benz et al. (1986; 1987; 1989) and Cameron and Benz (1991) performed numerical simulations of such impacts using the smoothed particle hydrodynamics method. Their main assumption is that all of the angular momentum of the Earth-Moon system is brought about by the single impact; in other words, they assumed the proto-Earth did not rotate at first. From this assumption Benz et al. estimated the size of the object (which hereafter we call the impactor) which collided with the proto-Earth and concluded that the impactor must be, at least, as large as Mars. The depletion of the iron in the Moon suggests that the collision had happened after the core formation in both the proto-Earth and the impactor. The parameters used in their simulations are the mass of the impactor, the initial relative velocity, and the impact parameter.

They simulated for wide ranges of the parameters and found that only in restricted ranges of the parameters sufficient amount of debris from which the Moon is formed begins to orbit around the Earth and, then, the ejected materials are thrown into the stable orbit owing to the gravitational torque made by the arm-like structure of the proto-Earth and the destroyed impactor. Based on their simulations, Benz et al. concluded that there is scarcely a possibility that a Moon-sized clump is directly formed just after the impact. Rather, they considered that, after the impact, the sprayed materials form a disk around the proto-Earth. and that the Moon must accrete from the disk through the process analogous to the planetary formation in the solar nebula.

Although this hypothesis has been considered as a favorite candidate for the theory of the lunar origin, there are several serious defects. First, the debris orbiting around the proto-Earth comes mostly from the Mars-sized impactor. This feature is inconsistent with the geochemical constraint mentioned in Section 1.2 (5) that the depletion pattern of V, Cr, and Mn in the Moon shows siderophile characters at high pressure.

Moreover, as we mentioned in Section 1.1 (1), if a substantial part of the present angular momentum of the Earth-Moon system originated from the accumulation of planetesimals, the single impact assumption made by Benz et al. becomes groundless. If it were the case, to decrease the angular momentum brought by the impact, either the mass of the impactor or the impact parameter must be lowered. However, the results of Cameron and Benz (1991) suggests it is more difficult to put materials into orbits in both cases, although the numerical calculations are not completed yet.

(2) Capture hypothesis

Nakazawa et al. (1983) suggested that the Moon was first accreted on a heliocentric orbit and captured by the Earth through the gas drag of its primordial atmosphere. They solved the restricted three-body problem including the effect of the gas drag and discovered that if the Moon enters into Hill sphere, the sphere of gravitational influence, of the Earth with relatively low velocity, it can be decelerated owing to the gaseous drag and captured before it escapes from the Hill sphere.

The weak point of this hypothesis is that some aspects of the chemical composition of the Moon cannot be explained; There may be a possibility that the Moon was heated substantially and lost volatile elements from its surface region (*e.g.*, owing to the tidal heating), or a possibility that both objects accreted at almost the same distance from the Sun gathering materials with the similar oxygen isotopic composition. However, in this hypothesis it is very difficult to remove large amount of iron from the Moon.

(3) Binary accretion hypothesis

In this hypothesis, it is postulated that the Moon is born as a "sister" of the Earth through the "co-accretion" process. This idea was first proposed by Ruskol (1961; 1963) and developed by Harris and Kaula (1975). They postulated that the Moon was accreted from a disk around the Earth and grew with the Earth. This framework is the same with the terrestrial planet formation. As in the case of planetary formation, the embryo of the Moon was formed by the gravitational instability of the disk around the proto-Earth. Then, both the proto-Earth and the proto-Moon grew through the collisions of planetesimals.

In order to explain the difference in chemical compositions between the Earth and the Moon, there must be a process to reduce iron from the disk and gather silicates preferentially. Moreover, to deplete volatile elements, some mechanisms to heat up the proto-Moon are needed. But any plausible processes for these problems have not been proposed yet.

(4) Fission hypothesis

At the end of the 19th century, George Howard Darwin (1879) first proposed that a part of the Earth was torn to form the Moon. He treated the Earth as a rotating spheroid composed of an incompressible fluid. At first, the Earth was rotating in a period about 5 hours. Then the free oscillation of Earth might be in resonance with the tide raised by the Sun, and then the large distortion can be produced to disrupt the proto-Earth. But Jeffreys (1930) pointed out that viscosity of the terrestrial mantle prevents the break up because it damps out the resonant oscillation.

Darwin (1880) also proposed another type of fission for the lunar origin. If the proto-Earth is rotating very fast, namely, in a period about 2 to 4 hours, the proto-Earth cannot keep its equilibrium figure and then the Moon can be split from the proto-Earth. The detail of this process is described in the next section. Ringwood (1960) reformed Darwin's hypothesis. Namely, according to the core formation, the moment of inertia of the proto-Earth decreases from 0.4 M_E R_E^2 to 0.33 M_E R_E^2 and the proto-Earth spins up. Ringwood considered this process might trigger the fission.

As we noted in the previous section, the rotational fission hypothesis is most preferable from the geochemical point of view. However, from the dynamical point of view, this hypothesis has several disadvantages. The most crucial defect is the problem of the angular momentum. In order that the rotational fission takes place, the total angular momentum must be about 4 times larger than that of the present Earth-Moon system. Furthermore, after the fission process completes, the excessive angular momentum has to be consumed by ejecting a part of materials from the Earth-Moon system. The finite inclination of the Moon is another weak point of this hypothesis because it is natural to consider that the rotational fission of the Moon occurs in the equatorial plane of the proto-Earth.

1.4. Review of Previous Works

The geochemical constraints imply that the materials from which the Moon was formed came from the magma ocean of the proto-Earth. The depth and the temperature of the magma ocean, under which the chemical compositions most resemble to those of the Moon, are estimated 300 km and 1600 °C, respectively (Okuchi, 1995). Since the giant impact cannot strip off the magma ocean, we must seek a different mechanism to tear off enough materials to form the Moon into orbits around the proto-Earth. The rotational fission is still one of the candidates, although it has several difficulties to overcome. Let us in this section review the investigations which are concerned with the rotational fission hypothesis of the Moon in detail.

(1) The Maclaurin spheroid

The equilibrium figures of rotating, self-gravitating bodies composed of incompressible fluid have been studied since the 17th century. The classical results are summarized by Chandrasekhar (1969). Newton first studied this subject in the latter half of the 17th century. He found that the body becomes an oblate spheroid owing to the centrifugal force. Maclaurin generalized this result and derived the relation between the eccentricity of the spheroid e and the rotational angular velocity Ω:

$$\frac{\Omega^2}{\pi G \rho} = \frac{2\sqrt{1-e^2}}{e^3}\left(3-2e^2\right)\sin^{-1} e - \frac{6}{e^2}\left(1-e^2\right) \quad , \tag{1.3}$$

where G is the gravitational constant and ρ is the density of the body. This type of spheroid was named the Maclaurin spheroid after him; Eq. (1.3) is called the Maclaurin's formula. In Fig. 1.3, the relation between Ω^2 and e is shown. As the rotational angular velocity increases, the spheroid becomes more oblate, *i.e.*, the eccentricity becomes large. At a point where the eccentricity reaches a certain critical value e_{c1}, not only the Maclaurin spheroid, but also the triaxial ellipsoid called the Jacobi ellipsoid is also admitted as an equilibrium figure. Because the gravitational energy of the Jacobi ellipsoid is smaller than that of the Maclaurin spheroid, if there exists some energy dissipation process such as viscosity, the Maclaurin spheroid deforms gradually into the Jacobi ellipsoid. This phenomenon is called "the secular instability" and this point e_{c1} is called the bifurcation point.

If the rotational angular velocity increases in a short time, bifurcation to the Jacobi ellipsoid does not occur. The spheroid only becomes more and more oblate. When the eccentricity of the spheroid reaches e_{c2} (where $e_{c2} > e_{c1}$), the Maclaurin spheroid becomes dynamically unstable to the perturbation which elongates or shortens the spheroid toward the horizontal direction. This means that the body can no longer keep the equilibrium figure.

The Jacobi ellipsoid also becomes more elongate as the rotational angular velocity increases. Then, at the point where

$$a_2/a_1 = 0.432232, \quad a_3/a_1 = 0.345069, \quad \text{and} \quad \Omega^2/\pi G\rho = 0.28403 \quad , \tag{1.4}$$

it deforms into the pear like shape called the Poincaré figure (a_i denotes semiaxis of the ellipsoid). However, the Poincaré figure is dynamically unstable and we regard that the fission occurs at this point. In Table 1.1, we summarize the values of the angular momentum where the instabilities described above take place compared to the value of the current Earth-Moon system.

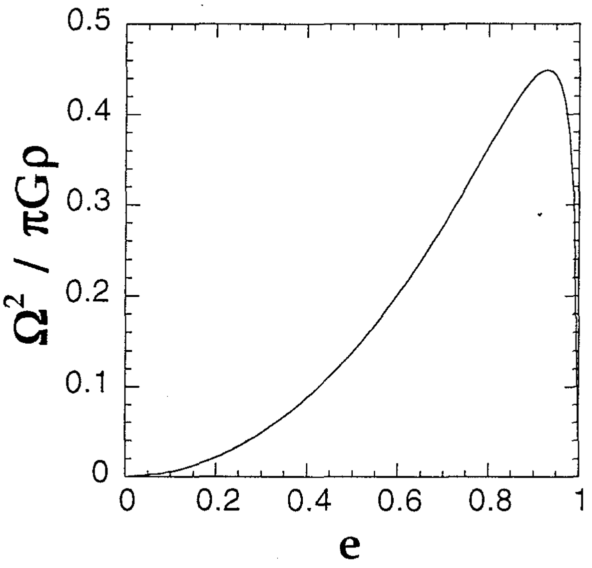

Fig. 1.3. The variation of the square of the angular velocity Ω^2 against the eccentricity e of the Maclaurin spheroid. The angular velocity is measured in the unit of $(\pi G\rho)^{1/2}$ where ρ is the density of the body.

(2) Further development of models of rotating bodies

Development of computers enables us to investigate directly the equilibrium figure as well as the process of fission by means of numerical calculations. Eriguchi and Sugimoto (1981) constructed a powerful method to seek equilibrium figures of rotating incompressible bodies. Using this method, Eriguchi and Hachisu (1983, 1985) found several sequences of equilibrium figures which branch off from the Maclaurin sequence. Further, Eriguchi and Müller (1985) extended the method to the equilibrium figure for which the equation of state is written by the polytropic relation

$$p \propto \rho^{1+1/n} \quad , \tag{1.5}$$

where p is the pressure and n is a parameter called the polytropic index.

The numerical simulation of the fission process after the dynamical instability was investigated by Durisen and Scott (1984). They dealt with inviscid polytropic fluids and reached

Table 1.1. The critical angular momentum at which the instabilities of the incompressible body set in. The angular momenta are scaled by the value of the current Earth-Moon system.

	Angular Momentum
Current Earth-Moon System	1
Secular Instability (Maclaurin to Jacobi)	2.64
Dynamical Instability (Poincaré)	3.39
Dynamical Instability (Maclaurin)	4.43

almost the same results as in the case of incompressible fluids. Their results show that the binary fission by which the body breaks up into two parts does not occur. Instead, materials are sprayed around the central body. Boss and Mizuno (1984; 1985) investigated the dynamical instability taking into account the effect of the viscosity. They used the effective viscosity of 10^{15} poise and found that there was no tendency toward fission. In other words, viscous shear damps out the perturbations which lead to the dynamical instability.

Boss (1986) simulated the evolution of the uniformly rotating, axisymmetric, viscous polytropic body with $n = 1/2$ after a sudden increase in the rotational angular velocity. The value of the polytropic index corresponds approximately to the compressibility of the Earth. He found that the body begins to lose materials from its equator before reaching dynamical instability. The materials released from the body forms a torus and moves outward. Hereafter, we call this phenomenon "the mass-shedding." A similar process occurs for the incompressible bodies. Eriguchi et al. (1982) observed the mass-shedding from an incompressible pear-shape body.

1.5. The purpose of this work

The main purpose of this work is to clarify whether the instability which leads to the fission of the highly rotating body can occur when the inhomogeneity of the proto-Earth is taken into account. There are two different approaches to the problem: one is to assume an arbitrarily continuous density distribution (Boss, 1986) and the other is to treat the mantle and the core as incompressible fluids with different densities. We will adopt the latter approach: we suppose that the proto-Earth is composed of two incompressible fluids whose densities are ρ_0 and $\rho_1 = \rho_0 + \delta\rho$. There are two important parameters in our model: one is the ratio of the volume of the core, V_1, to that of the proto-Earth, V_0, and the other is the ratio of the density increment in the core, $\delta\rho$, to the density of the mantle, ρ_0. To investigate the stability, we first seek numerically an equilibrium figure of the body assuming that it is axisymmetric with respect to the rotational axis. Then, by the use of the linear perturbation method, we examine the stability of the equilibrium figure against small perturbations.

In Chapter 2, we will find approximately equilibrium figures assuming that both the body surface and the core-mantle boundary of the proto-Earth are spheroidal. The numerical procedure to find accurately equilibrium figures of the two-layered incompressible bodies will be given in Chapter 3. Our method is an extension of the method developed by Eriguchi and Sugimoto (1981). The equilibrium figures, obtained numerically for various range of $\delta\rho/\rho_0$ and V_1/V_0, will be described in Chapter 4. Chapter 5 will concern the stability of the equilibrium figures using the criterion derived by Chandrasekhar and Lebovitz (1962). Application to the lunar origin will be discussed in Chapter 6.

2. Approximate Approach to the Solutions

In this chapter we will seek approximately equilibrium figures of two-layered bodies in a semi-analytical manner assuming that the geometrical figures of the body surface and the core-mantle boundary are spheroidal. This approximate approach is based on the tensor analysis used in the study of homogeneous rotating liquid bodies (e.g., Chandrasekhar, 1969). The validity of this approach will be quoted at the end of this chapter.

2.1. Basic formulation

Suppose that a gravitating system with uniform rotation is composed of two layers with different density. Hereafter, these two layers will be called a mantle and a core, for convenience. In this chapter, we will make, for simplicity, the following assumptions:

(1) Both the mantle and the core are composed of incompressible fluids; their densities are ρ_0 and $\rho_0 + \delta\rho$, respectively.

(2) The rotational angular velocity Ω is constant throughout the system.

(3) The system is axi-symmetric with respect to its rotational axis.

(4) The shapes of the body-surface and the core-mantle boundary are both spheroidal (such a system will be called a double-layered spheroid).

In Fig. 2.1, we illustrate a geometrical configuration of the system considered in this chapter schematically. The volume of the whole body and the core are denoted by V_0 and V_1, respectively. As seen from Fig. 2.1, the semi-axes of the body surface are denoted by a_1 and a_3 and those of the core-mantle boundary by a_1' and a_3'. Then, their eccentricities are defined as

$$e_0 = \sqrt{1 - \left(\frac{a_3}{a_1}\right)^2} \tag{2.1}$$

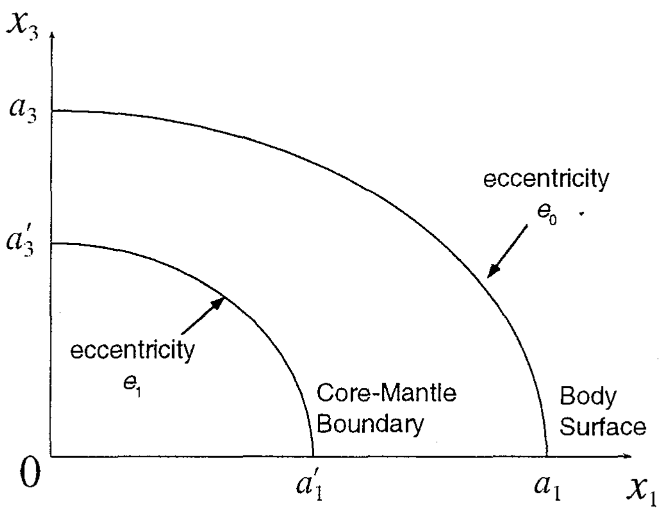

Fig. 2.1. Geometrical configuration of the system considered in this chapter.

and

$$e_1 = \sqrt{1 - \left(\frac{a_3'}{a_1'}\right)^2} \quad . \tag{2.2}$$

For convenience, we will define the following quantities:

$$\tilde{a}_1' = \frac{a_1'}{a_1} \tag{2.3}$$

and

$$\tilde{a}_3' = \frac{a_3'}{a_3} \quad . \tag{2.4}$$

With $\tilde{a}_3'$ and $\tilde{a}_3$, the eccentricity of the core-mantle boundary can be rewritten as

$$e_1 = \sqrt{1 - \left(\frac{\tilde{a}_3'}{\tilde{a}_1'}\right)^2 \left(\frac{a_3}{a_1}\right)^2} = \sqrt{1 - \left(\frac{\tilde{a}_3'}{\tilde{a}_1'}\right)^2 (1 - e_0{}^2)} \quad . \tag{2.5}$$

In order to find the equilibrium figures of the system, we use the second-order virial equations. We choose the direction of rotation along the x_3-axis (see Fig. 2.1) and set the origin of the coordinate system at the figure center of the body. Then the relevant equations can be given in a complex form by (Chandrasekhar, 1969)

$$W_{ij} + \Omega^2 \left(I_{ij} - \delta_{i3}\, I_{3j}\right) = -\delta_{ij} \prod \quad . \tag{2.6}$$

In the above, δ_{ij} is the Kronecker's delta and W_{ij} is the potential energy tensor defined as

$$W_{ij} = -\frac{1}{2} \, G \int_{\mathrm{V}} \int_{\mathrm{V}} \rho(\mathbf{x}) \, \rho(\mathbf{x}') \, \frac{(x_i - x_i')\,(x_j - x_j')}{|\mathbf{x} - \mathbf{x}'|^3} d\mathbf{x} \, d\mathbf{x}' \quad , \tag{2.7}$$

where G denotes the gravitational constant and subscript V annexed to the integral symbol means that the integral is to be performed over the whole volume of the system. Furthermore, I_{ij} is the moment of inertia tensor

$$I_{ij} = \int_{\mathrm{V}} \rho(\mathbf{x}) \; x_i \, x_j \; d\mathbf{x} \tag{2.8}$$

and $\prod$ is the 0-th order moment of pressure p, *i.e.*,

$$\prod = \int_{\mathrm{V}} p \; d\mathbf{x} \quad . \tag{2.9}$$

Note that Einstein's abbreviation rule is never used throughout this paper, *i.e.*, we do not take summation over repeated indices.

By noting the symmetry of the system, we readily find that the non-diagonal components of Eq. (2.6) are trivially satisfied, *i.e.*, six of nine components of Eq. (2.6) can be ignored. Among the remaining three equations, (1, 1)-component and (2, 2)-component are identical because of the symmetry of the system. Therefore, only two diagonal components are independent. They are given by

$$W_{11} + \Omega^2 \, I_{11} = W_{33} = -\prod \quad . \tag{2.10}$$

Solving these equations with respect to the square of the angular velocity Ω^2, we have

$$\Omega^2 = \frac{W_{33} - W_{11}}{I_{11}} \quad . \tag{2.11}$$

This will be called 'the equation of the equilibrium condition' in the following sections.

2.2. Evaluation of the potential energy tensor

In the present case, the potential energy tensor W_{ij}, defined by Eq. (2.7), can be divided into three parts:

$$W_{ij} = W_{ij}^0 + W_{ij}^1 + W_{ij}^* \tag{2.12}$$

where

$$W_{ij}^{0} = -\frac{1}{2}\, G\, {\rho_0}^2 \int_{V_0}\int_{V_0} \frac{(x_i - x_i')\,(x_j - x_j')}{|\mathbf{x} - \mathbf{x}'|^3}\, d\mathbf{x}\, d\mathbf{x}' \quad , \tag{2.13}$$

$$W_{ij}^{1} = -\frac{1}{2}\, G\, (\delta\rho)^2 \int_{V_1}\int_{V_1} \frac{(x_i - x_i')\,(x_j - x_j')}{|\mathbf{x} - \mathbf{x}'|^3}\, d\mathbf{x}\, d\mathbf{x}' \quad , \tag{2.14}$$

and

$$W_{ij}^{*} = -G\delta\rho\, \rho_0 \int_{V_1}\int_{V_0} \frac{(x_i - x_i')\,(x_j - x_j')}{|\mathbf{x} - \mathbf{x}'|^3}\, d\mathbf{x}\, d\mathbf{x}' \quad . \tag{2.15}$$

Note that subscripts V_0 and V_1 in Eqs. (2.13) to (2.15) denote, respectively, the volume surrounded by the body surface (but not the volume of the mantle) and that surrounded by the core-mantle boundary (*i.e.*, the volume of the core). Accordingly, W_{ij}^{0} denotes the potential energy tensor of a homogeneous spheroid of which volume and density are V_0 and ρ_0, respectively. Whereas, W_{ij}^{1} denotes the same tensor of a homogeneous spheroid of which volume and density are V_1 and $\delta\rho$, respectively. On the other hand, W_{ij}^{*} presents the potential energy tensor originated from the gravitational interaction between two spheroids with V_0 (and ρ_0) and V_1 (and $\delta\rho$).

Thus, both W_{ij}^{0} and W_{ij}^{1} can be readily integrated (Chandrasekhar, 1969) :

$$W_{ij}{}^{k} = -2\,\pi\, G\, (\rho_k - \delta_{1k}\rho_0)\, A_i(e_k)\, I_{ij}^{k} \quad , \quad k = 0 \text{ or } 1. \tag{2.16}$$

It is noted that $(\rho_k - \delta_{1k}\rho_0)$ in the above equation reduces simply to ρ_0 and $\delta\rho$ ($= \rho_1$ - ρ_0) for the cases of $k = 0$ and 1, respectively. Furthermore, $A_i(e)$ are called index symbols and are functions only of the eccentricity, e. For an oblate spheroid, these are written as

$$A_1(e) = A_2(e) = \frac{\sqrt{1 - e^2}}{e^3} \sin^{-1} e - \frac{1 - e^2}{e^2} \quad , \tag{2.17}$$

and

$$A_3(e) = \frac{2}{e^2} - \frac{2\sqrt{1 - e^2}}{e^3} \sin^{-1} e \quad . \tag{2.18}$$

Furthermore, the moment of inertia tensor I_{ij}^{k}, which is similarly defined as Eq. (2.8), is expressed in this case as

$$I_{ij}^{0} = \frac{1}{5}\, M^0\, a_i^2\, \delta_{ij} \quad \text{and} \quad I_{ij}^{1} = \frac{1}{5}\, M^1\, a_i'^2\, \delta_{ij} \quad , \tag{2.19}$$

where M^0 and M^1 are the masses of the spheroids given, respectively, by

$$M^0 = \rho_0 V_0 \quad \text{and} \quad M^1 = \delta\rho V_1 \quad . \tag{2.20}$$

In order to evaluate W^*_{ij}, we first consider the following integral over the volume V_0:

$$\frac{U^0_{ij}}{\pi G \rho_0} = \int_{V_0} \frac{(x_i - x'_i)\ (x_j - x'_j)}{|\mathbf{x} - \mathbf{x}'|^3}\, d\mathbf{x}' \quad . \tag{2.21}$$

Noting that $\mathbf{x}$ is a coordinate vector of an internal point of the spheroid, we find that the tensor potential U^0_{ij} can be written by the following form (Chandrasekhar, 1969):

$$\frac{U^0_{ij}}{\pi G \rho_0} = 2B^0_{ij}\ x_i\ x_j + a_i{}^2 \delta_{ij} \left(A^0_{ij} - \sum_{l=1}^{3} A^0_{il}\ x_l{}^2 \right) \quad . \tag{2.22}$$

In the above, index symbols A^0_{ij} and B^0_{ij} are defined, respectively, by

$$A^0_{ij} = \int_0^\infty \frac{du}{\Delta\ (a_i{}^2 + u)\ (a_j{}^2 + u)} \tag{2.23}$$

and

$$B^0_{ij} = \int_0^\infty \frac{u\ du}{\Delta\ (a_i{}^2 + u)\ (a_j{}^2 + u)} \quad , \tag{2.24}$$

where

$$\Delta = \sqrt{(a_1{}^2 + u)\ (a_2{}^2 + u)\ (a_3{}^2 + u)} \quad . \tag{2.25}$$

For an oblate spheroid, we find

$$A^0_{11} = A^0_{22} = \frac{1}{4\ a_1{}^2\ e_0{}^4} \left\{ 3\ \frac{\sqrt{1 - e_0{}^2}}{e_0} \sin^{-1} e_0 - \left(1 - e_0{}^2\right) \left(3 + 2e_0{}^2\right) \right\} \quad , \tag{2.26}$$

$$A^0_{33} = \frac{2\sqrt{1 - e_0{}^2}}{a_1{}^2\ e_0{}^4} \left\{ \frac{\sqrt{1 - e_0{}^2}}{e_0} \sin^{-1} e_0 - \frac{3 - 4e_0{}^2}{3\sqrt{1 - e_0{}^2}} \right\} \quad , \tag{2.27}$$

$$B^0_{11} = B^0_{22} = \frac{1}{4\ e_0{}^4} \left\{ \left(4e_0{}^2 - 3\right) \frac{\sqrt{1 - e_0{}^2}}{e_0} \sin^{-1} e_0 - \left(1 - e_0{}^2\right) \left(4 - 3e_0{}^2\right) \right\} \quad , \tag{2.28}$$

and

$$B^0_{33} = \frac{2}{e_0{}^4} \left\{ \frac{\sqrt{1 - e_0{}^2}}{e_0} \sin^{-1} e_0 + 3 - e_0{}^2 \right\} \quad . \tag{2.29}$$

Integrating $\delta\rho\ U^0_{ij}$ over the volume of the core V_1, we finally obtain

$$\frac{W^*_{ij}}{\pi G \rho_0} = 2\ B^0_{ij}\ I^1_{ij} + {a_i}^2\ \delta_{ij}\ \left(\delta\rho\ V_1\ A^0_{ij} - \sum_{l=1}^{3} A^0_{il}\ I^1_{ll}\right) \quad . \tag{2.30}$$

It should be noted that the total moment of inertia tensor I_{ij}, defined by Eq. (2.8), is presented by the sum of the two tensors defined previously:

$$\begin{aligned} I_{ij} &= I^0_{ij} + I^1_{ij} \\ &= I^0_{ij}\left(1 + \tilde{a}'^4_1\ \tilde{a}'_3\ \frac{\delta\rho}{\rho_0}\right) \end{aligned} \tag{2.31}$$

2.3. Boundary conditions

Only when the equi-pressure surface coincides with the surface where the total potential $\Phi_{\rm t}(\mathbf{x})$ is constant, the body is in the state of gravitational equilibrium. Furthermore, the total potential must be constant at the core-mantle boundary, otherwise the body becomes unstable against Rayleigh-Taylor instability (see *e.g.*, Chandrasekhar, 1961). Consequently, the boundary conditions to be imposed are written by

$$\begin{cases} \Phi_{\rm t}(\mathbf{x}) = \text{constant} & \text{at the body surface} \\ \Phi_{\rm t}(\mathbf{x}) = \text{constant} & \text{at the core-mantle boundary.} \end{cases} \tag{2.32}$$

The total potential $\Phi_{\rm t}(\mathbf{x})$ is defined by

$$\Phi_{\rm t}(\mathbf{x}) = \Phi_{\rm g}(\mathbf{x}) + \Phi_{\rm c}(\mathbf{x}) \quad , \tag{2.33}$$

where $\Phi_{\rm g}(\mathbf{x})$ is the gravitational potential given by

$$\Phi_{\rm g}(\mathbf{x}) = \int_{\rm V} \frac{\rho(\mathbf{x}')}{|\mathbf{x} - \mathbf{x}'|}\ d\mathbf{x}' \tag{2.34}$$

and $\Phi_{\rm c}(\mathbf{x})$ is the centrifugal potential given by

$$\Phi_{\rm c}(\mathbf{x}) = \frac{1}{2}\ \Omega^2\ \varpi^2 \tag{2.35}$$

because of the assumption of the uniform rotation (in the above, ϖ is the distance from the rotational (x_3-) axis).

Using index symbols introduced in the preceding section, the gravitational potential $\Phi_g(\mathbf{x})$ at a point $\mathbf{x}$ on the core-mantle boundary is written as

$$\Phi_g(\mathbf{x}) = \pi G \rho_0 \sum_{l=1}^{3} A_l(e_0) \left(a_l^2 - x_l^2\right) + \pi G \delta\rho \sum_{l=1}^{3} A_l(e_1) \left(a_l'^2 - x_l^2\right) . \quad (2.36)$$

On the other hand, the gravitational potential at the surface of the spheroid can be written, by using Ivory's theorem, as (Chandrasekhar, 1969)

$$\begin{aligned} \Phi_g(\mathbf{x}) &= \pi G \rho_0 \sum_{l=1}^{3} A_l(e_0) \left(a_l^2 - x_l^2\right) \\ &+ \pi G \delta\rho\, a_1'^2 a_3' \int_0^\infty \frac{du}{\left(a_1'^2 + \lambda + u\right)\sqrt{\left(a_3'^2 + \lambda + u\right)}} , \end{aligned} \quad (2.37)$$

where λ is the larger root of the quadratic equation

$$\frac{x_1^2}{a_1'^2 + \lambda} + \frac{x_3^2}{a_3'^2 + \lambda} = 1 \quad (2.38)$$

and λ is called the ellipsoidal coordinate. Although we write down the expression of $\Phi_g(\mathbf{x})$ at the surface of the spheroid (*i.e.*, Eq. (2.37)) to give completeness to the mathematical description, this equation is not used, as will be seen in the next section, in our study except in the last section of this chapter. So, we do not mention further development of the expression of Eq. (2.37).

2.4. Equations to be solved

The equilibrium figure of the body can be completely determined by seven variables, the equatorial radius of the body a_1, the eccentricity of the body surface e_0, the equatorial radius of the core a_1', the eccentricity of the core-mantle boundary e_1, the density of the mantle ρ_0, the density of the core $\rho_0 + \delta\rho$, and the angular velocity Ω. Among these seven variables, a_1, ρ_0, $\delta\rho$, and Ω are given as the physical parameters. In certain formulas, we also give the volume ratio V_1/V_0 as a variable, since there is a relation among the eccentricity of the core-mantle boundary, e_1, the axis ratio, a_1'/a_1, and the volume ratio, V_1/V_0, *i.e.*,

$$\frac{V_1}{V_0} = \tilde{a}_1'^2\, \tilde{a}_3' = \tilde{a}_1'^3 \sqrt{\frac{1 - e_1^2}{1 - e_0^2}} , \quad (2.39)$$

the number of unknown quantities is only two. Therefore, we are able to find an equilibrium figure of a double-layered spheroid by the use of the equilibrium condition (*i.e.*, Eq. (2.11)) and one of the two boundary conditions (see Eq. (2.32)). This is due to the adopted assumption that both the body surface and the core-mantle boundary are spheroidal (remember that, for the case of the Maclaurin spheroid, the figure is determined only by the equilibrium condition without any boundary condition, because the equilibrium condition and the boundary condition at the body surface are identical).

Inserting W_{11}, W_{33}, and I_{11} derived in the preceding section into Eq. (2.11) and eliminating e_1 by the use of Eq. (2.5), we obtain

$$\begin{aligned}
\frac{\Omega^2}{\pi G\rho_0}\left(1+\tilde{a}_1'^4\tilde{a}_3'\frac{\delta\rho}{\rho_0}\right) &= \frac{2}{e_0^2}\left\{\sqrt{1-e_0^2}\left(3-2e_0^2\right)\frac{\sin^{-1}e_0}{e_0}-3(1-e_0^2)\right\}\\
&+ 2\left(\frac{\delta\rho}{\rho_0}\right)^2\frac{\tilde{a}_1'^4\tilde{a}_3'^2\sqrt{1-e_0^2}}{\tilde{a}_1'^2-\tilde{a}_3'^2(1-e_0^2)}\\
&\times\left[\left\{\tilde{a}_1'^2+2\tilde{a}_3'^2\left(1-e_0^2\right)\right\}\frac{\sin^{-1}\sqrt{1-(1-e_0^2)\tilde{a}_3'^2/\tilde{a}_1'^2}}{\sqrt{\tilde{a}_1'^2-\tilde{a}_3'^2(1-e_0^2)}}-3\tilde{a}_3'\sqrt{1-e_0^2}\right]\\
&+\frac{\delta\rho}{\rho_0}\tilde{a}_1'^2\tilde{a}_3\frac{\sqrt{1-e_0^2}}{e_0^4}\\
&\times\left[\frac{\sin^{-1}e_0}{e_0}\left\{5e_0^2(3-2e_0^2)+\tilde{a}_1'^2(8e_0^2-9)+\tilde{a}_3'^2(9-2e_0^2)(1-e_0^2)\right\}\right.\\
&\qquad\left.+\sqrt{1-e_0^2}\left\{-15e_0^2+\tilde{a}_1'^2(9-2e_0^2)+\tilde{a}_3'^2(5e_0^2-9)\right\}\right]\ .
\end{aligned} \tag{2.40}$$

As a natural consequence, in the limit of $\delta\rho\to 0$ as well as in the limit of $\tilde{a}_3'\to 0$ and $\tilde{a}_3'/\tilde{a}_1'\to$ constant, Eq. (2.40) reduces to the Maclaurin's formula (see Eq. (1.3))

$$\frac{\Omega^2}{\pi G\rho_0} = \frac{2\sqrt{1-e_0^2}}{e_0^3}\left(3-2e_0^2\right)\sin^{-1}e_0-\frac{6}{e_0^2}\left(1-e_0^2\right)\quad . \tag{2.41}$$

Also, in the limit of $\tilde{a}_1'\to 1$ and $\tilde{a}_1'\to 1$, we obtain a resemble result.

Among the two boundary conditions, we choose the condition that the total potential is constant on the core-mantle boundary. Substituting the expressions of the gravitational potential and the centrifugal potential (*i.e.*, Eqs. (2.36) and (2.35)) into Eq. (2.33), we first write down the expression of the total potential explicitly. Then, equating $\Phi_t(x_1=x_2=0, x_3=a_3')$ with $\Phi_t(x_1=a_1', x_2=x_3=0)$ according to the boundary condition at the core-mantle boundary and eliminating e_1 as earlier, we have the relation between the square of the angular velocity and the eccentricity of the body surface e_0, that is,

$$
\begin{aligned}
\frac{\Omega^2}{\pi G \rho_0} = & \frac{2\sqrt{1-e_0^2}}{e_0^3} \sin^{-1} e_0 \left(1 + \frac{2\tilde{a}_3'^2}{\tilde{a}_1'^2}(1-e_0^2)\right) - \frac{2}{e_0^2}(1-e_0^2)\left(1 + \frac{2\,\tilde{a}_3'^2}{\tilde{a}_1'^2}\right) \\
& + 2\frac{\delta\rho}{\rho_0} \frac{\tilde{a}_1'^2 \tilde{a}_3' \sqrt{1-e_0^2}}{\tilde{a}_1'^2 - \tilde{a}_3'^2(1-e_0^2)} \\
& \times \left[-3\,\frac{\tilde{a}_3'}{\tilde{a}_1'^2}\,\sqrt{1-e_0^2} + \left\{1 + \frac{2\,\tilde{a}_3'^2}{\tilde{a}_1'^2}(1-e_0^2)\right\} \frac{\sin^{-1}\sqrt{1-(1-e_0^2)\,\tilde{a}_3'^2/\tilde{a}_1'^2}}{\sqrt{\tilde{a}_1'^2 - \tilde{a}_3'^2\,(1-e_0^2)}}\right] .
\end{aligned}
\tag{2.42}
$$

Equations (2.39), (2.40), and (2.42) are the equations to be solved simultaneously, that govern the equilibrium figure of the double-layered spheroid. In our present study, we solve these equations by means of the Newton-Raphson method.

2.5. Equilibrium figures of the double-layered spheroids

The meridional cross sections for the cases of $e_0 = 0.5$ and 0.8 are shown, respectively, in Fig. 2.2 (a) and 2.2 (b). In both cases, we take $V_1/V_0 = 1/8$ and $\delta\rho/\rho_0 = 1$. These figures show that the body surface and the core-mantle boundary are quite similar, namely, the eccentricity of the core-mantle boundary, e_1, is almost equal to that of the body surface, e_0. In order to see in detail the relation between e_1 and e_0, we show the variation of e_1 in Fig. 2.3 as a function of e_0. As seen from this figure, e_1 is always smaller than e_0 and the difference $e_0 - e_1$ becomes larger with an increase in e_0. But it does not exceed 0.075 as long as $V_1/V_0 = 1/8$ and $\delta\rho/\rho_0 = 1$. It may be interesting to see how the $e_0 - e_1$ relation depends on the parameters V_1/V_0 and $\delta\rho/\rho_0$. To do so, we expand (2.40) and (2.42) into a power series of e_1^2 and e_0^2 assuming that e_0^2, $e_1^2 \ll 1$ and retain the lowest order terms. Furthermore, eliminating Ω^2 from the two resultant equations, we have

$$
e_1 = \sqrt{\frac{5\ (1 + V_1\delta\rho/V_0\rho_0)}{5 + \delta\rho/\rho_0\left\{2 + 3\,(V_1/V_0)^{5/3}\right\}}}\ e_0 \quad . \tag{2.43}
$$

The above equation shows that, as the first approximation, e_1 is proportional to e_0 and that e_1/e_0 does not deviate largely from 1 regardless of the adopted values of $\delta\rho/\rho_0$ and V_1/V_0.

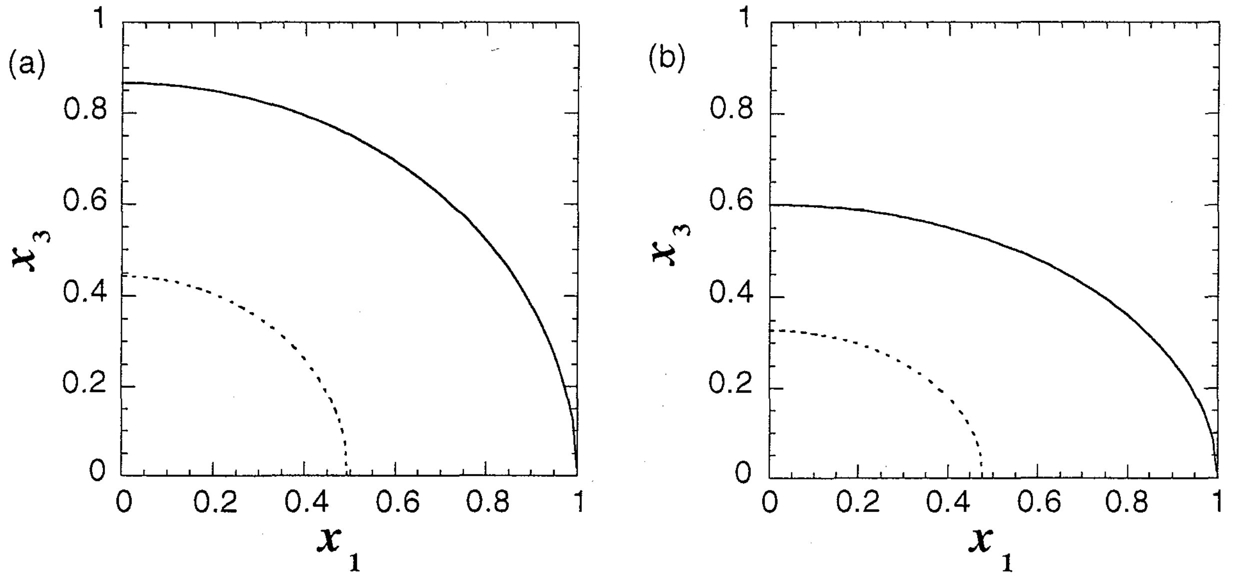

Fig. 2.2. The meridional cross sections of the equilibrium figures of the double layered spheroids in the case of $V_1/V_0 = 1/8$ and $\delta\rho/\rho_0 = 1$: (a) $e_0 = 0.5$, (b) $e_0 = 0.8$, where e_0 denotes the eccentricity of the body surface.

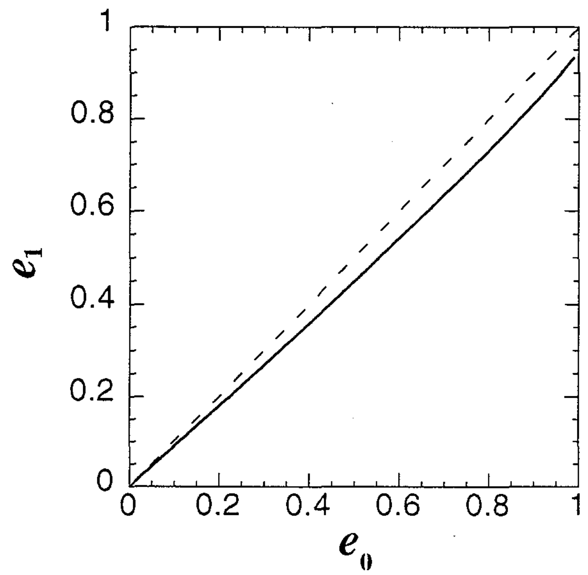

Fig. 2.3. The relation between the eccentricity of the core e_1 and that of the body surface e_0. The values of V_1/V_0 and $\delta\rho/\rho_0$ are taken to be 1/8 and 1, respectively.

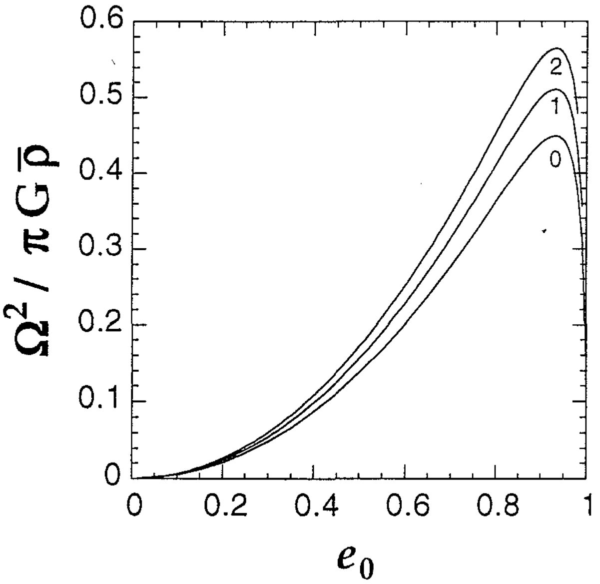

Fig. 2.4. The variation of the square of the angular velocity Ω^2 against the eccentricity of the body surface e_0 in the case of V_1/V_0 =1/8. The curves are attached by the values of $\delta\rho/\rho_0$.

When $\delta\rho/\rho_0 = 1$ and $V_1/V_0 = 1/8$, Eq. (2.43) yields $e_1 = 0.92\ e_0$ which is almost identical to the e_1-e_0 relation obtained numerically (*i.e.*, the solid line in Fig. 2.3).

The square of the angular velocity is illustrated in Fig. 2.4 for the case of $V_1/V_0 = 1/8$. To compare the result with that of the Maclaurin Spheroid, we measure Ω in the unit $(\pi G\overline{\rho})^{1/2}$ where $\overline{\rho}$ is the mean density of the spheroid given by

$$\overline{\rho} = \rho_0 \left(1 + \frac{\delta\rho}{\rho_0}\frac{V_1}{V_0}\right) \quad . \tag{2.44}$$

For the case $\delta\rho/\rho_0 = 0$ (*i.e.*, the curve attached by 0), the curve coincides exactly with that of the Maclaurin spheroid. This is quite a natural consequence. When $\delta\rho/\rho_0 > 0$, the curve is shifted upward. Namely, at the same eccentricity, the angular velocity for the two-layered spheroid is apparently larger than that of Maclaurin spheroid. This feature can be understood as follows: with an increase in the degree of central condensation of mass (but the constant mean density, $\overline{\rho}$), the gravity force at the equator becomes large and, hence, the strong centrifugal force, *i.e.*, the high angular velocity Ω, is needed to maintain the same spheroidal

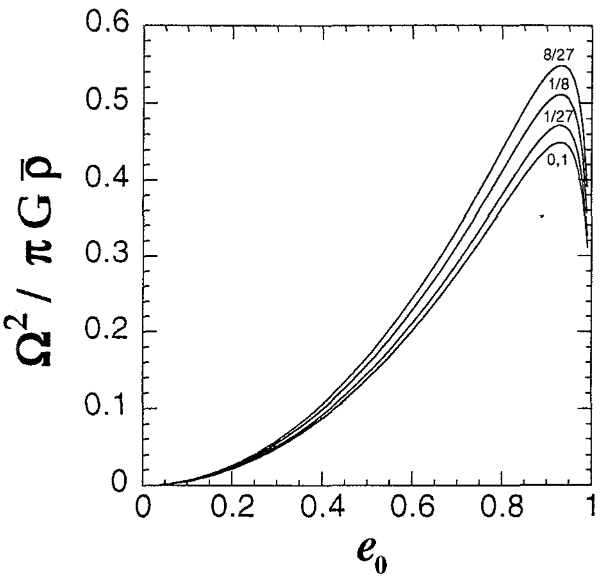

Fig. 2.5. The variation of the square of the angular velocity Ω^2 against the eccentricity of the body surface e_0 for various values of the volume ratio V_1/V_0. The values of $\delta\rho/\rho_0$ is taken to be 1.

figure.

From an alternative point of view, we show the Ω^2 - e_0 relation in Fig. 2.5 for a fixed $\delta\rho/\rho_0$ ($= 1$) and various values of V_1/V_0. When $V_1/V_0 = 1$ and 0, the curve coincides with that of the Maclaurin spheroid since the spheroid is homogeneous in both cases. With an increase in V_1/V_0, the curve departs upward from that of the Maclaurin spheroid. But its deviation reaches the maximum at a certain value of V_1/V_0 and then goes down toward that of the Maclaurin spheroid. Such a behavior is explicitly demonstrated in Fig. 2.6, in which Ω^2 is shown as a function of V_1/V_0 for the case of $\delta\rho/\rho_0 = 1$ and $e_0 = 0.7$. Namely, $\Omega^2/\pi G\overline{\rho}$ is equal to the value of the Maclaurin spheroid, 0.277, at $V_1/V_0 = 0$ and 1 and takes its maximum value at $V_1/V_0 \sim$ 0.35 (note that the value of V_1/V_0, at which $\Omega^2/\pi G\overline{\rho}$ becomes maximum, depends weakly on the adopted value of $\delta\rho/\rho_0$).

Finally, we show the total angular momentum L for the various cases of V_1/V_0 in Fig. 2.7. The angular momentum L is measured in the unit of $(GM^3\overline{a})^{1/2}$ where $\overline{a}$ is the radius of the

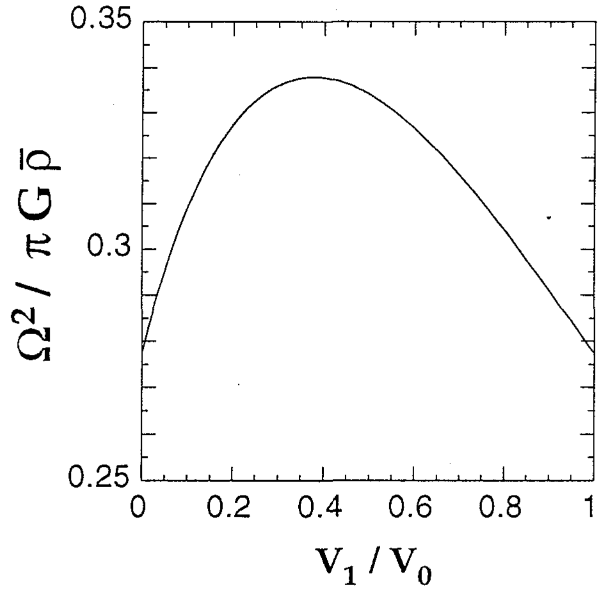

Fig. 2.6. The relation between the square of the angular velocity Ω^2 and the volume ratio V_1/V_0 for a fixed eccentricity of the body surface e_0 (= 0.7). As in the case of Fig. 2.5, $\delta\rho/\rho_0$ is taken to be 1.

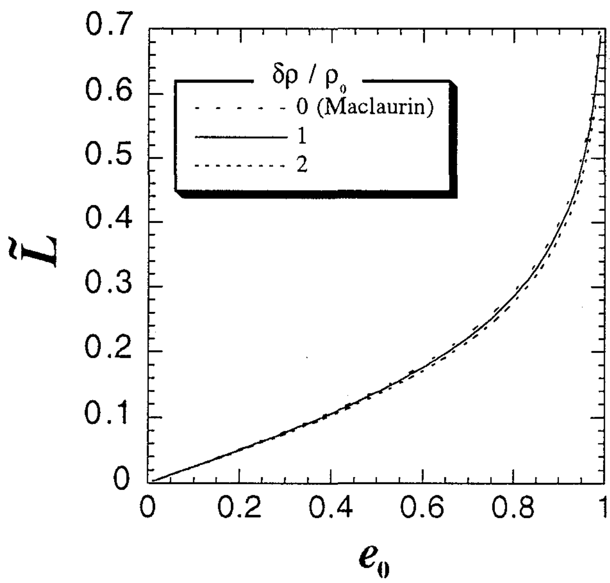

Fig. 2.7. The normalized angular momentum $\tilde{L}$ as a function of eccentricity of the body surface e_0 in the case of $V_1/V_0 = 1/8$ (as for the normalization, see text). The curves are attached by the values of $\delta\rho/\rho_0$.

sphere of which mass is equal to the total mass of the spheroid M. This unit is equal to the angular momentum of the grazing satellite with mass M orbiting circularly around the body. For the same eccentricity, the value of $\widetilde{L}$ for the two-layered spheroid are slightly smaller than that of the Maclaurin spheroid but the difference is very small. This is due to a decrease in the moment of inertia for the double-layered spheroid.

2.6. Validity of this method

As mentioned in section 2.4, we have three equations which govern the equilibrium state of the double-layered spheroid, namely, Eqs. (2.40), (2.42), and the first equation of Eq. (2.32). Among these three equations we used the first two equations to find the equilibrium figure assuming, a priori, that the last equation is automatically satisfied, at least, in an approximate manner. Strictly speaking, the three equations quoted above are not consistent with each other. This comes from the fact that even if the core-mantle boundary is spheroidal the external equi-potential surface generated by the core is not spheroidal (note that the internal equi-potential surface forms a spheroid). So, only when the three equations are satisfied simultaneously within an accuracy of a certain level, then the obtained result is admissible as an approximate equilibrium figure of the double-layered spheroid.

Thus, we can see the validity of the present approximation by knowing how accurately the third (remaining) equation, *i.e.*, the first equation of Eq. (2.32), is satisfied. Here, as a practical manner, we evaluated the difference between the values of the total potential $\Phi_{\rm t}$ at the pole and at the equator of the spheroid; The difference may be measured by the form of the relative error δ defined as

$$\delta = \frac{\left|(\Phi_{\rm t})_{\rm pole} - (\Phi_{\rm t})_{\rm equator}\right|}{\left|(\Phi_{\rm t})_{\rm equator}\right|} . \tag{2.45}$$

At the equator of the spheroid, *i.e.*, at a point $(x_1, x_3) = (a_1, 0)$, the ellipsoidal coordinate λ (the largest root of Eq. (2.38)) is equal to $a_1^2 - a_1'^2$. Then, we can readily evaluate the integral on the right hand side of Eq. (2.37) and we have the total potential at the equator of the

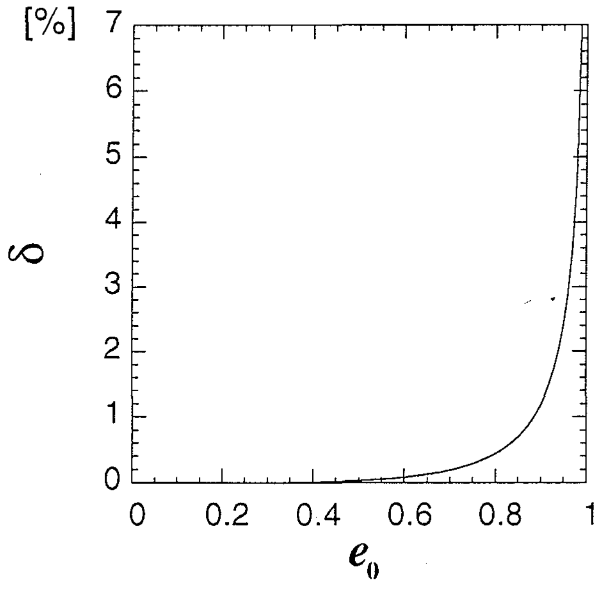

Fig. 2.8. The relative error δ between the total potential at the equator and that at the pole against the eccentricity of the body surface e_0.

spheroid

$$(\Phi_t)_{\text{equator}} = \frac{1}{2}\,\Omega^2\,{a_1}^2 + \pi\,G\,\rho_0\,\left\{\,A_1(e_0)\,a_1^2 \;+\; A_3(e_0)\,a_3^2\,\right\}$$
$$+\pi\,G\,\delta\rho\,a_1'^2\,\sqrt{1-e_1^2}\left[\frac{2}{e_1}\left\{1-\frac{a_1^2}{2a_1'^2e_1^2}\right\}\sin^{-1}\left(\frac{a_1'e_1}{a_1}\right)-\frac{\sqrt{a_1^2-a_1'^2e_1^2}}{a_1'e_1^2}\right] \quad , \tag{2.46}$$

where $A_i(e)$ is the index symbols defined by Eqs. (2.17) and (2.18). Similarly, at the pole of the spheroid, *i.e.*, at a point $(x_1,\,x_3) = (0,\,a_3)$, the ellipsoidal coordinate λ is equal to $a_3^2 - a_3'^2$ and we have

$$(\Phi_t)_{\text{pole}} = 2\,\pi\,G\,\rho_0\,A_1(e_0)\,a_1^2$$
$$+2\,\pi\,G\,\delta\rho\,a_1'^2\,\sqrt{1-e_1^2}\left[\frac{1}{e_1}\left\{1+\frac{a_3^2}{a_1'^2e_1^2}\right\}\sin^{-1}\left(\frac{a_1'e_1}{\sqrt{a_3^2+a_1'^2e_1^2}}\right)+\frac{a_3}{a_1'e_1^2}\right] \quad . \tag{2.47}$$

We show the variation of δ against the eccentricity of the body surface e_0 in Fig. 2.8. The error is negligibly small when the eccentricity of the body surface e_0 is small. However, as e_0 exceeds 0.8, the error becomes apparent and when e_0 becomes large beyond 0.9, the error exceeds 1 %. For other sets of V_1/V_0 and $\delta\rho/\rho_0$ we have the similar results. Thus we can say that the two-layered homogeneously rotating body can be well approximated by the double-layered spheroid as long as we are concerned with a case where $e_0 \leq 0.8$. When the eccentricity becomes large, *i.e.*, when the effect of rotation is efficient, then we must seek another method to obtain the equilibrium figure. The validity check of this method will be presented more exactly in Chapter 4.

3. Accurate Approach to the Solutions

In this chapter we will present the numerical method to look accurately for the gravitational equilibrium figures of two-layered bodies without any restriction on the geometry of the body surface and the core-mantle boundary. Our method of calculation is an extension of the one formulated by Eriguchi and Sugimoto (1981), which they used in the study of the equilibrium figures of the gravitating bodies composed of a uniform incompressible fluid.

3.1. Assumptions

We are now considering gravitating bodies with two-layered structure, *i.e.*, the core and the mantle. The schematic picture of the body is illustrated in Fig. 3.1 together with the adopted coordinates. In the present study, we have made the following assumptions for the sake of simplicity:

(1) Both the mantle and the core are constituted from incompressible fluids of which densities are ρ_0 and ρ_1 ($= \rho_0 + \delta\rho$), respectively.

(2) The rotational angular velocity Ω is constant throughout the body.

(3) The equilibrium figure is axi-symmetric and plane-symmetric with respect to the rotation axis and the equatorial plane, respectively.

Assumptions (1) to (3) are quite the same as those adopted in Chapter 2. Note that, however, in this chapter we do not impose any restriction on the geometrical figures of the body surface as well as the core-mantle boundary.

In the present study we use the spherical polar coordinates (r, θ, φ) of which origin is placed at the center of mass of the body. Owing to assumption (3), the radial distances of the body surface and the core-mantle boundary can be completely determined by r and μ ($= \cos\theta$). Or,

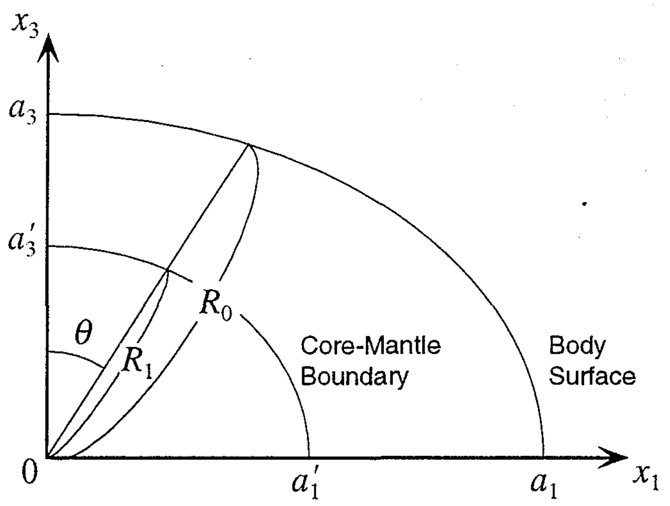

Fig. 3.1. Geometrical configuration of the system considered in this chapter.

in other words, the body surface and the core-mantle boundary are described by the followings:

$$\begin{cases} r = R_0(\mu) & \text{at the body surface,} \\ r = R_1(\mu) & \text{at the core-mantle boundary.} \end{cases} \tag{3.1}$$

Here, we assume that R_0 and R_1 are single-valued and monotonically decreasing functions of μ. For the sake of later convenience, we introduce the following quantities:

$$\epsilon = \sqrt{1 - (a_3/a_1)^2} \quad , \tag{3.2}$$

and

$$\eta = a'_1/a_1 \quad . \tag{3.3}$$

If the figure of the body surface is spheroidal, ϵ coincides with the eccentricity of a spheroid e_0 which is given by Eq. (2.1) in Chapter 2. Hereafter, ϵ is referred to as "the coaspect ratio" for simplicity.

3.2. Gravitational potential and equilibrium conditions

The gravitational potential $\Phi_g(r,\mu)$ is given by the well-known Newton's formula written by

$$\begin{aligned}
\Phi_g(r,\mu) &= -G \int d\mathbf{x}' \, \frac{\rho(r,\mu)}{|\mathbf{x}-\mathbf{x}'|} \\
&= -4\pi G \sum_{n=0}^{\infty} P_{2n}(\mu) \int_0^1 d\mu' \, P_{2n}(\mu') \int_0^{\infty} dr' \, r'^2 f(r,r') \, \rho(r',\mu') \ , \qquad (3.4)
\end{aligned}$$

where $P_{2n}(\mu)$ is the Legendre polynomials of rank $2n$ (note that the Legendre polynomials with odd rank disappear because of assumption (3)). Furthermore, $f(r,r')$ is a function of r and r' defined by

$$f(r,r') = \begin{cases} r'^{2n}/r^{2n+1} & \text{for } r \geq r' \ , \\ r^{2n}/r'^{2n+1} & \text{for } r < r' \ . \end{cases} \qquad (3.5)$$

Integration over r' can be readily executed and we find that the gravitational potential $\Phi_g(r,\mu)$ can be described by the sum of the potentials Φ_{g0} and Φ_{g1}: the former is due to the body with density ρ_0 and volume V_0 and the latter is due to the body with density $\delta\rho$ and volume V_1. Namely, we have

$$\Phi_g(r,\mu) = \Phi_{g0}(r,\mu) + \Phi_{g1}(r,\mu) \ , \qquad (3.6)$$

where

$$\frac{\Phi_{g0}(r,\mu)}{4\pi G\rho_0} = \sum_{n=0}^{\infty} P_{2n}(\mu) \int_0^1 d\mu' \, P_{2n}(\mu') \, h(r, R_0(\mu'); n) \qquad (3.7)$$

and

$$\frac{\Phi_{g1}(r,\mu)}{4\pi G\rho_0} = \frac{\delta\rho}{\rho_0} \sum_{n=0}^{\infty} P_{2n}(\mu) \int_0^1 d\mu' \, P_{2n}(\mu') \, h(r, R_1(\mu'); n) \ . \qquad (3.8)$$

In the above, $h(r,r';n)$ is a function defined by

$$h(r,r';n) = \int_0^{r'} dr'' \, r''^2 \, f(r,r'') \ . \qquad (3.9)$$

Or, more explicitly, $h(r, r'; n)$ is expressed as

$$h(r, r'; n) = \begin{cases} \frac{1}{2n+3} \frac{r'^{2n+3}}{r^{2n+1}} & \text{for } r \leq r', \\ r^2 \left(\frac{1}{2n+3} + \frac{1}{2n-2}\right) - \frac{1}{2n-1} \frac{r'^{2n+3}}{r^{2n+1}} & \text{for } r < r' \text{ and n} \neq 1, \\ r^2 \left(\frac{1}{5} + \ln \frac{r'}{r}\right) & \text{for } r < r' \text{ and } n = 1 \end{cases} . \quad (3.10)$$

Especially, the gravitational potential at the body surface is given by

$$\frac{\Phi_{g0}(R_0, \mu)}{4\pi G \rho_0} = \sum_{n=0}^{\infty} P_{2n}(\mu) \int_0^1 d\mu' \, P_{2n}(\mu') \, h(R_0(\mu), R_0(\mu'); n) \quad (3.11)$$

and

$$\frac{\Phi_{g1}(R_0, \mu)}{4\pi G \rho_0} = \frac{\delta\rho}{\rho_0} \sum_{n=0}^{\infty} P_{2n}(\mu) \int_0^1 d\mu' \, P_{2n}(\mu') \, h(R_0(\mu), R_1(\mu'); n) \quad . \quad (3.12)$$

Also the gravitational potential at the core-mantle boundary can be written in similar forms:

$$\frac{\Phi_{g0}(R_1, \mu)}{4\pi G \rho_0} = \sum_{n=0}^{\infty} P_{2n}(\mu) \int_0^1 d\mu' \, P_{2n}(\mu') \, h(R_1(\mu), R_0(\mu); n) \quad (3.13)$$

and

$$\frac{\Phi_{g1}(R_1, \mu)}{4\pi G \rho_0} = \frac{\delta\rho}{\rho_0} \sum_{n=0}^{\infty} P_{2n}(\mu) \int_0^1 d\mu' \, P_{2n}(\mu') \, h(R_1(\mu), R_1(\mu'); n) \quad . \quad (3.14)$$

The centrifugal potential Φ_c is simply given by Eq. (2.35):

$$\Phi_c(r, \mu, \Omega) = \Omega^2 \, \frac{r^2 \, (1 - \mu^2)}{2} \quad . \quad (3.15)$$

The gravitational equilibrium is achieved when the total potential Φ_t, *i.e.*, the sum of the gravitational potential $\Phi_g(r, \mu)$ and the centrifugal potential $\Phi_c(r, \mu, \Omega)$, is constant at the body surface as well as at the core-mantle boundary. Therefore, R_0 and R_1 must satisfy the following conditions:

$$\Phi_{g0}(R_0, \mu) + \Phi_{g1}(R_0, \mu) + \Phi_c(R_0, \mu, \Omega) = C_0 \quad (3.16)$$

and

$$\Phi_{g0}(R_1, \mu) + \Phi_{g1}(R_1, \mu) + \Phi_c(R_1, \mu, \Omega) = C_1 \quad , \quad (3.17)$$

where C_0 and C_1 are constants. These are the equilibrium equations to be solved.

3.3. Procedure of calculation

To find the solution to Eqs. (3.16) and (3.17) numerically, we divide the coordinate region of the colatitude (or, more exactly, cosine of the colatitude μ) into $N+1$ with an equal interval:

$$\mu_j = \frac{j}{N}, \qquad j = 0, 1, \ldots, \mathrm{N}. \tag{3.18}$$

Then, the corresponding radial distances of the body surface and the core-mantle boundary are given by

$$R_k^{(j)} = R_k(\mu_j) \qquad k = 0 \text{ or } 1, \tag{3.19}$$

where $k = 0$ and $k = 1$ denote, respectively, the values at the body surface and at the core-mantle boundary. For the sake of numerical convenience, the equatorial radius of the body $R_0^{(0)}$ is set to be 1.

We now consider Eqs. (3.16) and (3.17) only for the discrete $(N+1)$ points of μ given by Eq. (3.18). Then these equations become simultaneous equations of order $2N+2$. Unknown quantities are $R_0^{(j)}$ ($j = 1$ to N), $R_1^{(j)}$ ($j = 0$ to N), Ω, C_0, and C_1. While the number of equations is $2N+2$, the number of unknown quantities is $2N+4$. So, if two of the unknown quantities are given as parameters, then we can solve the equations. For convenience, we choose ϵ and η as the given parameters, which are defined by Eqs. (3.2) and (3.3), respectively: in the present case ϵ and η are presented, respectively, by

$$\epsilon = \sqrt{1 - \left(R_0^{(N)}\right)^2} \tag{3.20}$$

and

$$\eta = R_1^{(0)} \quad , \tag{3.21}$$

because $R_0^{(0)}$ is put to be 1.

To find the solutions we make use of the Newton-Raphson iteration scheme:

(1) We first assume the tentative values of R_0^j, R_1^j, Ω^2, C_0, and C_1, which are denoted by R_0^{j0}, R_1^{j0}, $(\Omega^2)^0$, C_0^0, and C_1^0, respectively.

(2) We substitute $R_0^j = R_0^{j0} + \delta R_0^j$, $R_1^j = R_1^{j0} + \delta R_1^j$, $(\Omega^2) = (\Omega^2)^0 + \delta(\Omega^2)$, $C_0 = C_0^0 + \delta C_0$, and $C_1 = C_1^0 + \delta C_1$ into Eqs. (3.16) and (3.17) and retain first order terms such as δR_0^j, δR_0^j, etc.

(3) Next we solve the simultaneous algebraic equations of order $2N+2$ by means of the usual matrix inversion method and find δR_0^j and δR_0^j, etc.

(4) Further we replace R_0^{0j}, R_1^{0j}, etc. by $R_0^{0j} + \delta R_0^j$, $R_1^{0j} + \delta R_1^j$, etc. and return to step (2) until δR_0^j, δR_1^j, etc. become sufficiently small.

We truncate the above procedure when the condition

$$\text{Max}\left[\frac{\delta R_0^j}{R_0^{0j}}, \frac{\delta R_1^j}{R_1^{0j}}, \frac{\delta(\Omega^2)}{(\Omega^2)^0}, \frac{\delta C_0}{C_0^0}, \frac{\delta C_1}{C_1^0}\right] < 10^{-4} \tag{3.22}$$

is satisfied. The approximate solutions presented in Chapter 2 are chosen for the initial tentative values of R_0^{j0}, R_1^{j0}, $(\Omega^2)^0$, C_0^0, and C_1^0.

In the present study, the number of division N in μ (see Eq. (3.18)) are taken to be 160. To check the accuracy of numerical calculations, we examined the case of $N = 320$ for several sets of ϵ and η and found that there were no obvious differences in the results between the cases of $N = 160$ and 320. For $N = 160$, the number of iterations necessary for obtaining a solution is at most 20. In many cases, we can arrive at a solution within five iterations.

In the evaluation of the potentials, Eqs. (3.11) to (3.14), we use the Simpson's method for the integration with respect to μ' and take the first 25 terms (at most) for the summation over n; more exactly, $n = 15$ for the case of $\epsilon \leq 0.8$ and $n = 25$ for the case of $\epsilon > 0.8$. In order to see the accuracy of this method, we calculated the gravitational potential of homogeneous spheroids and compared with the analytical solutions. In the cases where $N = 160$ and $e_0 < 0.95$, the relative error between numerical values and analytical values is kept within 0.1 percent.

As explained above, the parameters given in the calculation are ϵ and η. However, we are interested in solutions with a definite volume ratio $(V_1/V_0)^*$. So, we calculate the volume ratio

V_1/V_0 after the equilibrium figure is obtained for a fixed value of ϵ and a tentative value of η. If the evaluated ratio V_1/V_0 does not coincide with $(V_1/V_0)^*$, then we repeat the calculations changing η by 1/100, until we find the largest value of η satisfying the inequality $V_1/V_0 < (V_1/V_0)^*$ and the smallest η satisfying the inequality $(V_1/V_0)^* < V_1/V_0$. Then, evaluating the value of η which gives the desired volume ratio by means of the linear interpolation, we finally find the equilibrium figure for a desired set of ϵ and $(V_1/V_0)^*$.

4. Equilibrium Figures of Two-Layered Bodies

4.1. Meridional cross section of an equilibrium figure

We will first concentrate ourselves on the equilibrium figures of slowly rotating bodies. Hereafter, unless we note explicitly, the volume ratio V_1/V_0 and the density ratio $\delta\rho/\rho_0$ are taken to be 1/8 and 1.0, respectively.

The variation of the square of the angular velocity Ω^2 against the coaspect ratio ϵ, *i.e.*, the ratio of a_3 to a_1, is plotted in Fig. 4.1. In this figure, the approximate solutions obtained for the double-layered spheroids (see Chapter 2) are also shown in order to compare the results against each other. As in the case of the double-layered spheroids, Ω is scaled by the unit of $(\pi G\overline{\rho})^{1/2}$ where $\overline{\rho}$ is the mean density of the body given by Eq. (2.44):

$$\overline{\rho} \;=\; \rho_0 \left(1 \;+\; \frac{\delta\rho}{\rho_0}\frac{V_1}{V_0}\right) \quad . \tag{4.1}$$

The value of Ω^2 increases with an increase in ϵ when ϵ is small. It reaches its maximum at $\epsilon \sim 0.9$ and then decreases abruptly. This feature is the same with the Maclaurin spheroids (see Fig. 2.4). Furthermore, Ω^2 numerically obtained (solid lines) almost coincides with that of the double-layered spheroids (dashed lines) except where it reaches its maximum.

The meridional cross section of the equilibrium figure (*i.e.*, the figures in the x_1-x_3 plane) is shown in Fig. 4.2 (a) for the case where the coaspect ratio ϵ is equal to 0.2. The spheroidal surfaces with the same semimajor axis and the coaspect ratio (in this case, the eccentricity of the spheroid) are also plotted by the dashed curves in Fig. 4.2 (a). We also illustrate the view seen from the direction $\theta = 60°$ in Fig. 4.2 (b). As seen in Fig. 4.2 (a), when ϵ is as small as 0.2 (*i.e.*, when the rotation is slow), the figures of the body surface as well as the core-mantle boundary are completely fitted by spheroids.

When ϵ exceeds 0.8, the difference between the figure of the body surface and the spheroid with the eccentricity $e_0 = \epsilon$ becomes somewhat apparent as seen from Fig. 4.3 in which the

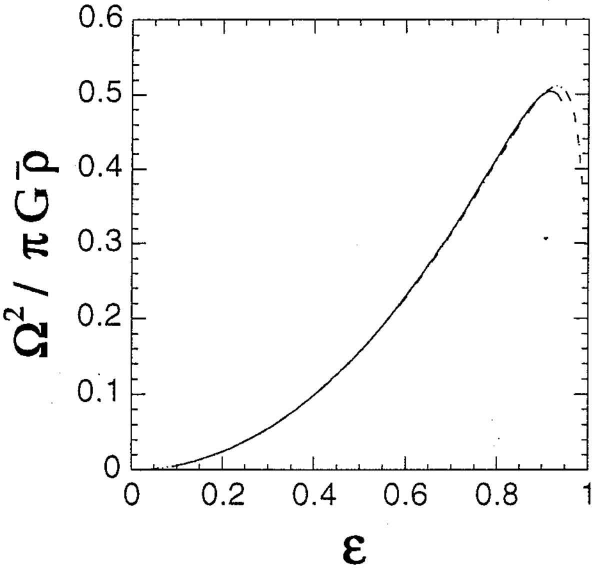

Fig. 4.1. The variation of the square of the angular velocity Ω against the coaspect ratio ϵ (the solid curve). The dashed curve corresponds to the approximate solutions for the double-layered spheroids.

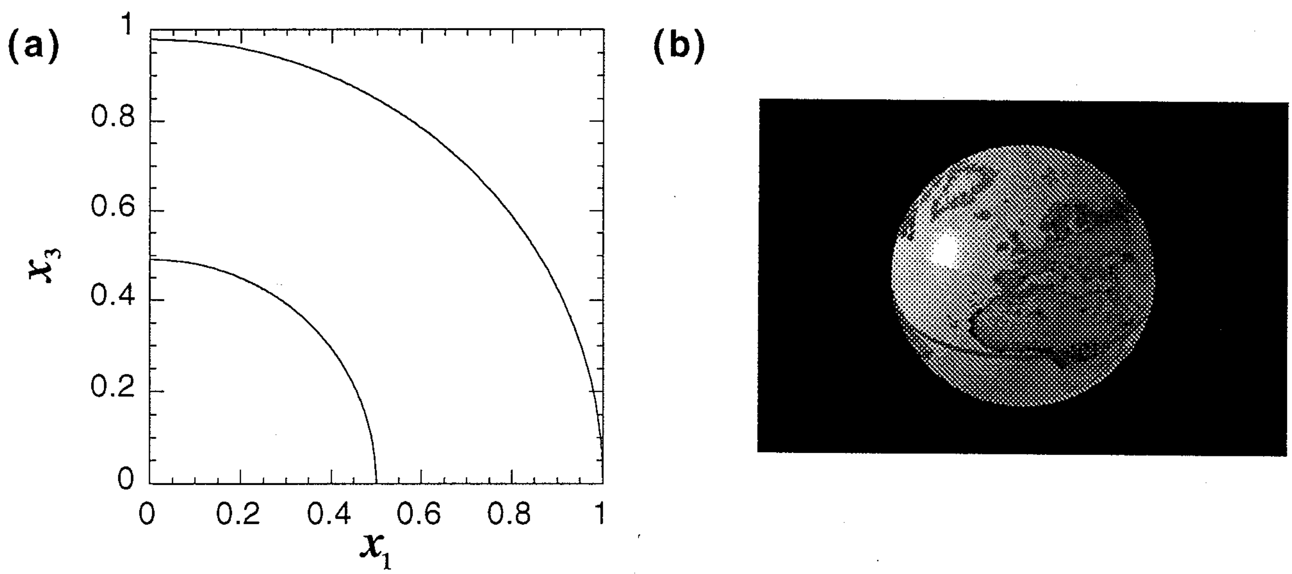

Fig. 4.2. (a) Meridional cross section for the case of $\epsilon = 0.2$. The spheroidal surfaces with the same semimajor axis and the coaspect ratio are also plotted by dashed curves. In this case, they almost coincide with each other. (b) The view shape for the same case seen from $\theta = 60°$.

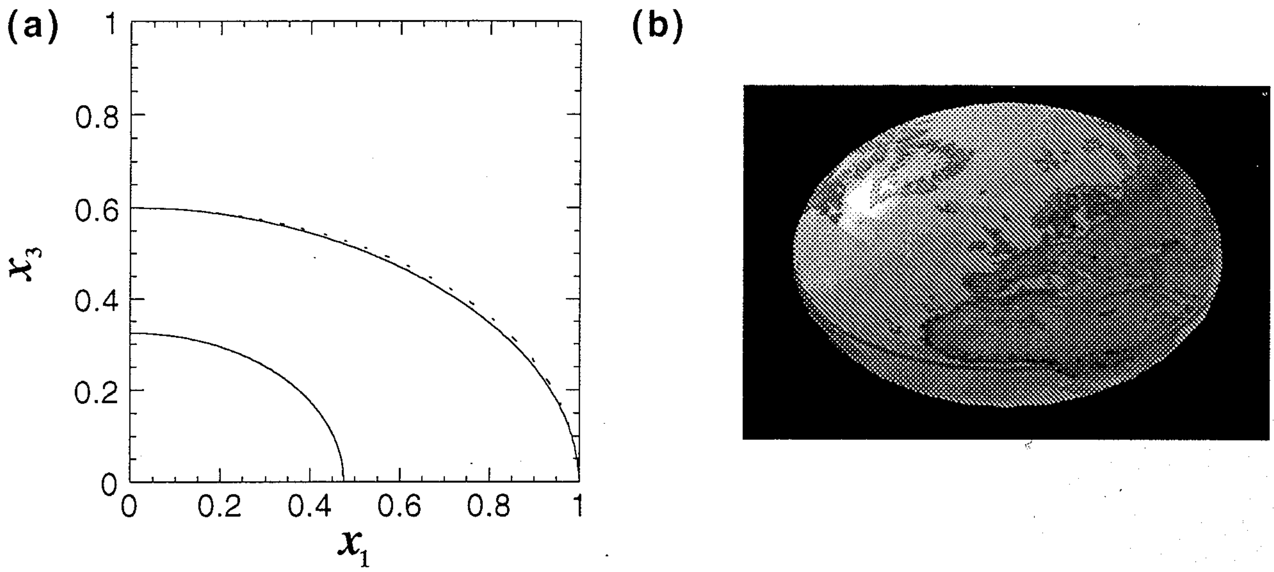

Fig. 4.3. The same as Fig 4.2, but for the case where $\epsilon = 0.8$.

meridional cross section is shown for the case of $\epsilon = 0.8$ together with the view seen from the direction $\theta = 60°$. We can see from this figure that the actual body surface is always under the spheroidal surface with the same eccentricity ϵ (dashed curve). The difference becomes largest at the 'mid-latitude' area. However, it is interesting to note that the figure of the core-mantle boundary is adequately approximated by the spheroidal surface. This is due to the fact that the centrifugal force acts more effectively on the body surface than on the core-mantle boundary. As ϵ increases further, the difference between the body surface and the spheroid becomes more distinct (see Fig. 4.4(a) for the case of $\epsilon = 0.9$) while the figure of the core-mantle boundary is almost spheroidal even in this case.

In Fig. 4.5, we plot the ratio of the core radius to the equatorial radius η as a function of ϵ. Unlike the angular velocity Ω which is shown in Fig. 4.1, the difference between the results of the present numerical calculations (dashed curve in Fig. 4.5) and of the double-layered spheroids (solid curve) becomes clear: the difference is very small when $\epsilon < 0.8$ but it increases distinctly when ϵ exceeds 0.8. This supports the previous result that the double-layered spheroids is a

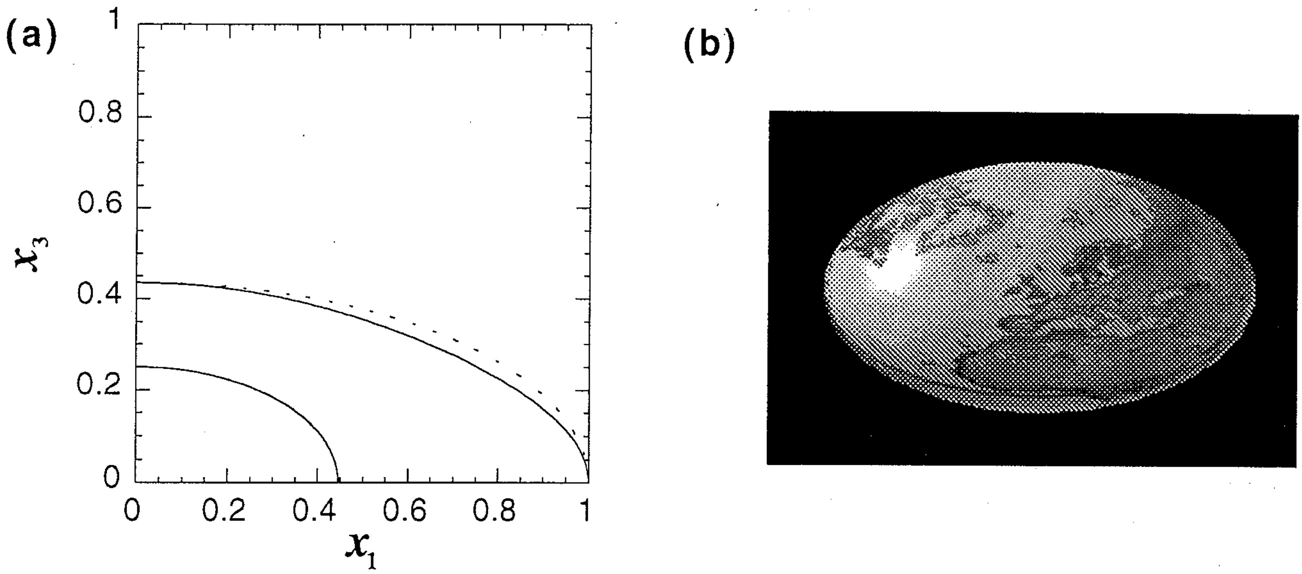

Fig. 4.4. The same as Fig 4.2, but for the case where $\epsilon = 0.9$.

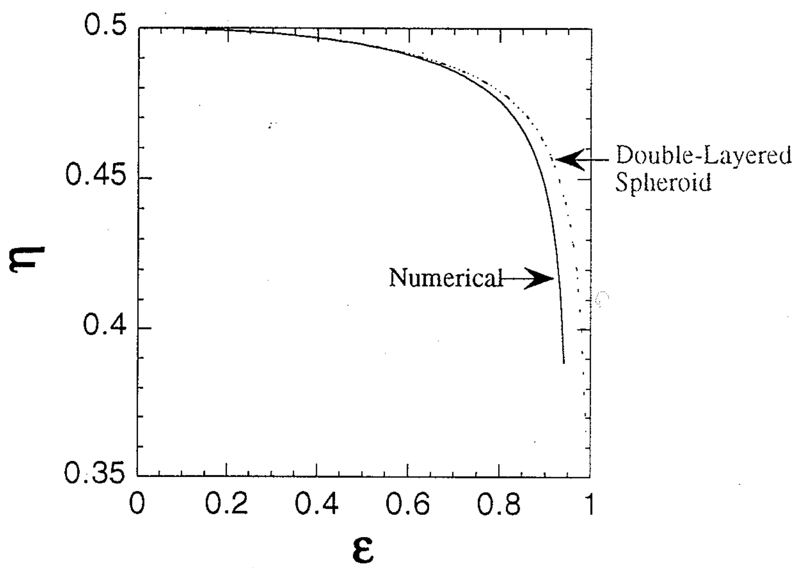

Fig. 4.5. The ratio of the core radius to the equatorial radius η against the coaspect ratio ϵ. The dashed line corresponds to the case of the double layered spheroid.

good approximation in the range where $e_0 < 0.8$.

By numerical calculations of various models we confirmed that such features quoted above are common irrespective of the adopted values of V_1/V_0 and $\delta\rho/\rho_0$. Thus we can conclude that the approximate approach mentioned in Chapter 2 due to the double-layered spheroid is valid as long as we are concerned with the case where the eccentricity of the body surface, e_0, is less than 0.8. Furthermore, when ϵ is greater than 0.8, the shape of the body surface deforms apparently from a spheroid so as to be suppressed in the vertical direction (*i.e.*, in the direction of the rotational axis), especially, at the mid-latitude area. We can also say that the core-mantle boundary is always well approximated by a spheroid.

4.2. Existence of the critical coaspect ratio

As seen in the previous section, when ϵ exceeds 0.8, the difference between the figure of the body surface begins to deviate appreciably from a spheroid. In addition to this geometrical feature in the region of high coaspect ratio, we find an interesting physical phenomenon which occurs between $\epsilon = 0.941$ and $\epsilon = 0.942$ through the numerical calculations of various models. The meridional cross sections of the equilibrium figures are shown in Figs. 4.6(a) and 4.6(b) for the cases of $\epsilon = 0.941$ and $\epsilon = 0.942$, respectively. In both cases, the body surface is largely suppressed toward the equatorial plane and deviates from a spheroidal surface. This can be seen from Fig. 4.7 in which a view shape seen from the direction $\theta = 60°$ is illustrated for the case of $\epsilon = 0.941$. Looking at Figs. 4.6(a) and 4.6(b) carefully, we also find that the figure at the equator behaves almost as a cusp when $\epsilon = 0.941$ and that the surface waves slightly in the vicinity of the equator when $\epsilon = 0.942$. To see in detail the surface region near the equator, we repeated the calculations with the same physical parameters V_1/V_0 and $\delta\rho/\rho_0$ but with the fine spatial division $N = 320$. Even in such calculations of models we found that the same surface feature appears near the equator.

In order to understand physically the surface structure near the equator, we will pay our

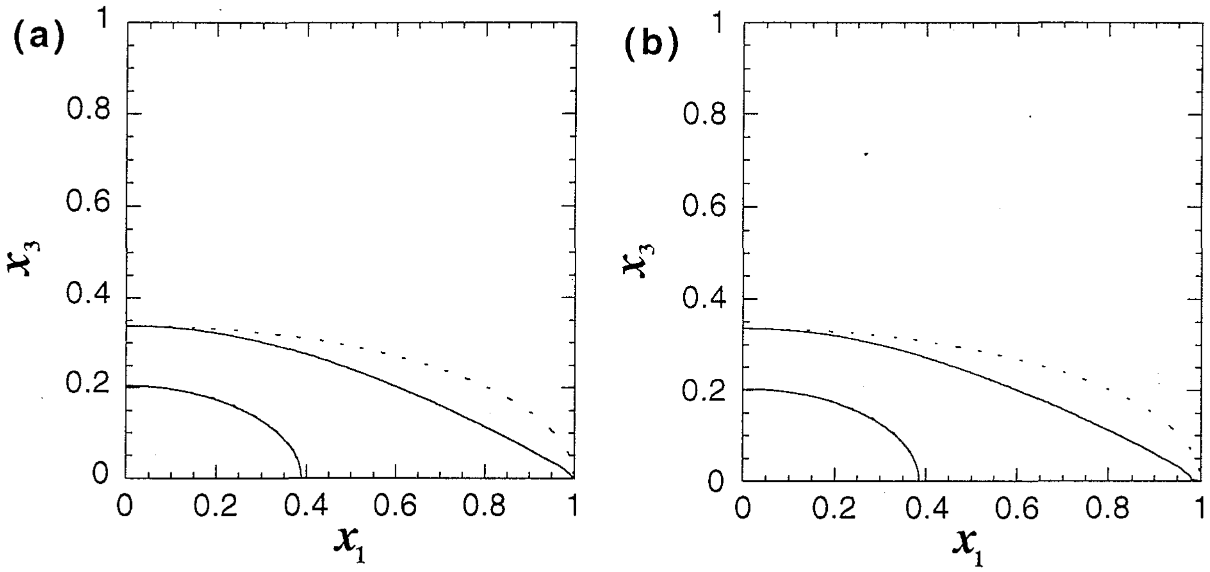

Fig. 4.6. (a) Meridional cross section for the case of $\epsilon = 0.941$. The dashed curves denote the spheroidal surfaces with the same semimajor axis and the coaspect ratio. (b) The same as figure (a) but for the case where $\epsilon = 0.942$. Note that the body surface shows an wavy structure near the equator.

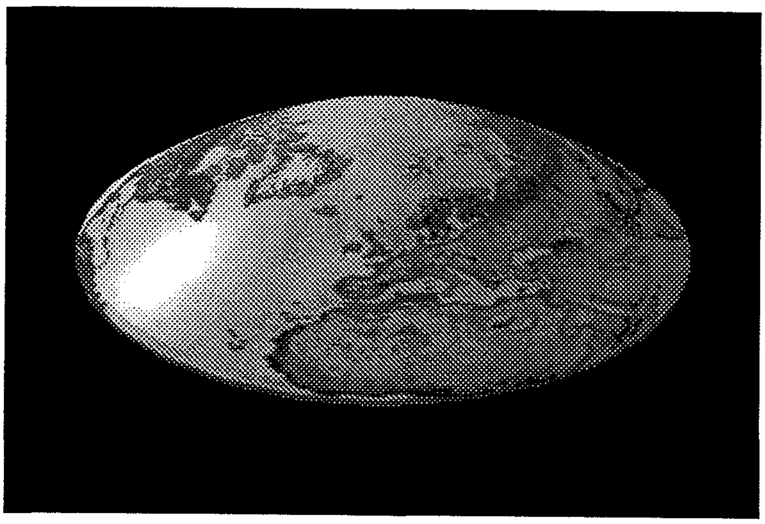

Fig. 4.7. The view shape for the case of $\epsilon = 0.941$ seen from $\theta = 60°$.

attention to the total potential Φ_t along the equatorial plane, which is shown in Fig. 4.8. For the case of $\epsilon = 0.941$, Φ_t is a monotonically increasing function of x_1 in the region $x_1 \leq 1$ (see Fig. 4.8(a) and (b)), though it varies very slowly for $x_1 \leq 0.5$ compared with the gravitational potential Φ_g (which being denoted by the dashed curve). It should be noted that the difference between Φ_g and Φ_t is, of course, due to the centrifugal potential. For the case of $\epsilon = 0.942$, the total potential Φ_t seems to behave, on the whole, by the same way that in the case of $\epsilon = 0.941$ (see Fig. 4.9(a)). But there is a point where $d\Phi_t/dx_1 = 0$ inside the body ($x_1 \sim 0.99$) for the case of $\epsilon = 0.942$ (see Fig. 4.9(b)). Outside the point, $d\Phi_t/dx_1$ becomes positive, *i.e.*, the total force acts toward the direction of the positive x_1. In this region of x_1, the outward centrifugal force overcomes the inward gravitational force. The point on the x_1-coordinate, which satisfies $d\Phi_t/dx_1 = 0$, will be hereafter called the neutral point. Let us consider the meaning of the wavy surface near the equator which is observed in Fig. 4.6(b). In Fig. 4.10, we illustrate the body surface obtained numerically (drawn by the solid curve) and the numerical grid points (denoted by the circles) together with the equi-potential surface (drawn by the dashed curve). The neutral point exists just inside the point A which denotes the equatorial radius ($x_1 = 1$) numerically found. On the other hand, the meridional cross section of the equi-potential surface runs through point B (see the dashed line in Fig. 4.10) but not point A; point A, at which the body surface crosses the equatorial plane, rests on another equi-potential surface with the same value of Φ_t. Thus, the wavy surface near the equator observed for the case of $\epsilon = 0.942$ is a result of the numerical misconnection of the equi-potential surface.

It is natural to consider that a stable gravitating body cannot include the neutral point inside the body surface. Namely, there exists a critical value of the coaspect ratio ϵ beyond which we have no equilibrium configuration as a single and axis-symmetric body. Such a coaspect ratio will be called the critical coaspect ratio and denoted by ϵ_c: If ϵ exceeds ϵ_c, *i.e.*, if the angular momentum of the body becomes larger than a certain critical value, no equilibrium figure exists as a single body with the following geometrical features:

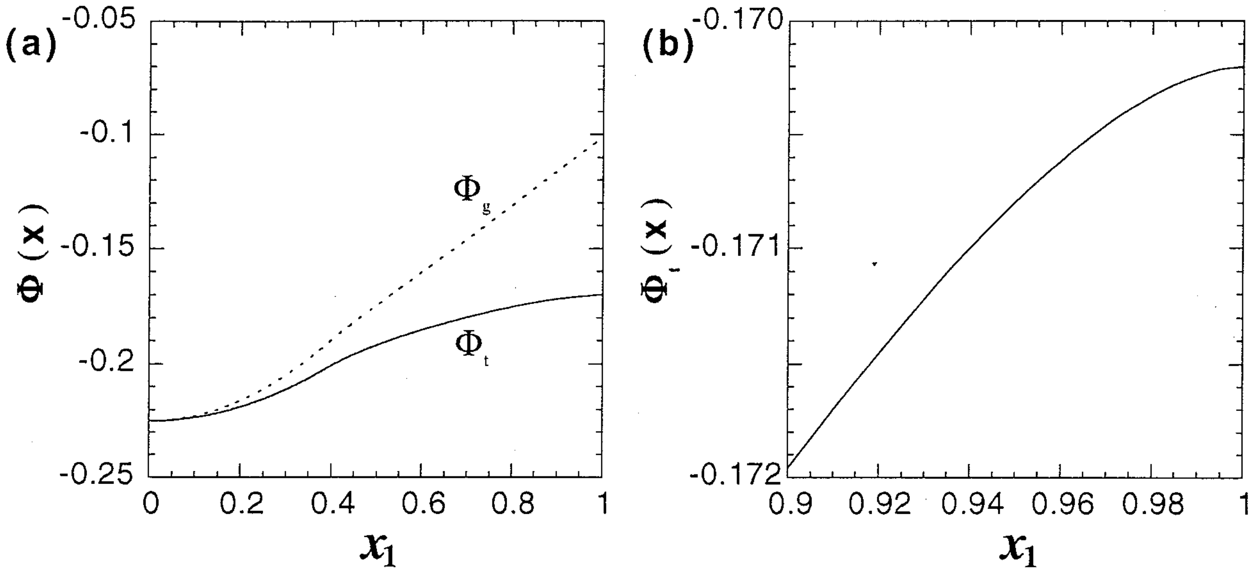

Fig. 4.8. (a) The variation of the total potential Φ_t and the gravitational potential Φ_g along the x_1-axis for the case where $\epsilon = 0.941$. (b) The magnified structure of (a) near the body surface.

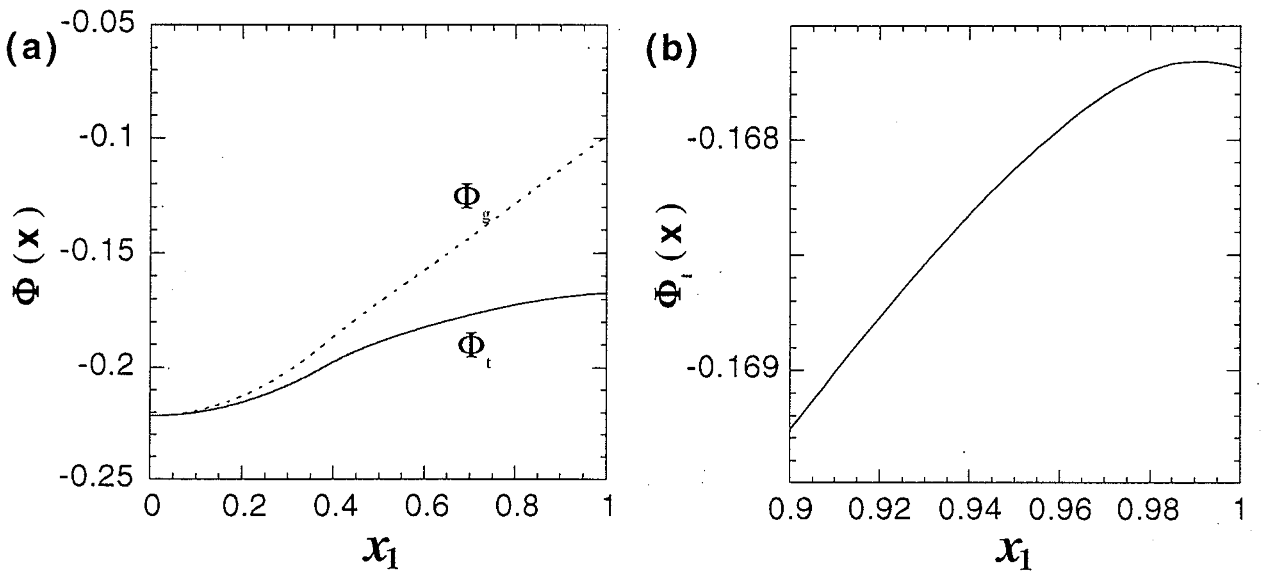

Fig. 4.9. (a) The same as Fig. 4.8 but for $\epsilon = 0.942$. (b) The magnified structure of (a) near the body surface.

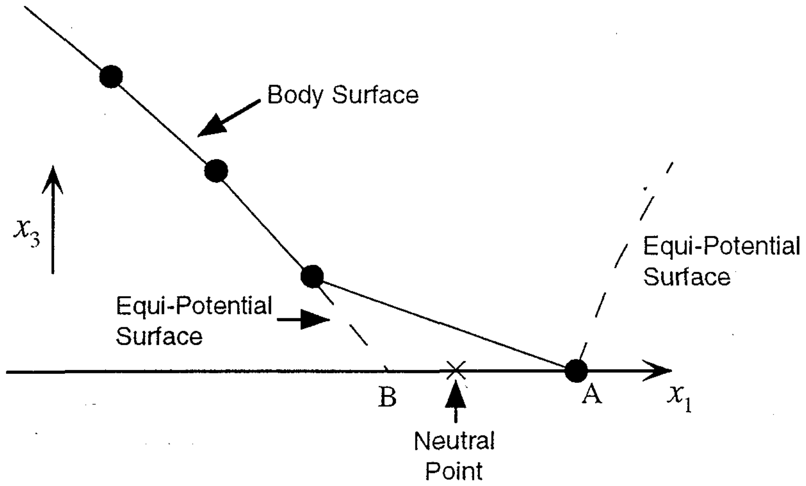

Fig. 4.10. The structure of the body surface (solid curve) and the equi-potential surface (dashed curve) near the equator in the case of $\epsilon = 0.942$.

(1) Axially symmetric with respect to its rotational axis,

(2) Symmetry with respect to its equatorial plane,

(3) The body surface R_0 and the core-mantle boundary R_1 being the single-valued and the monotonically decreasing functions of μ.

Note that, of course, existence of ϵ_c does not mean that any type of the equilibrium figures, *e.g.*, triaxial figures, toroids, and others, cannot exist.

From the above argument, we can readily find the condition which gives the critical coaspect ratio ϵ_c: when

$$d\Phi_{\rm t}/dx_1 = 0 \qquad \text{at } (x_1, x_3) = (1, 0) \tag{4.2}$$

is satisfied for a gravitating body, then the coaspect ratio ϵ of the body is just the critical coaspect ratio ϵ_c. We will argue more generally the critical aspect ratio in the last section of this chapter.

4.3. Angular velocity, angular momentum, and energy

In Fig. 4.11, we show the relation between the square of the angular velocity Ω^2 and the coaspect ratio ϵ for various values of $\delta\rho/\rho_0$. As before, Ω is measured in the unit $(\pi G\overline{\rho})^{1/2}$ and the volume ratio V_1/V_0 is still taken to be 1/8. The curve attached by 0 denotes the $\Omega^2 - \epsilon$ relation of the Maclaurin spheroid, $\delta\rho/\rho_0 = 0$. The curves are terminated at the critical coaspect ratios ϵ_c which are marked by the cross '×' in Fig. 4.11. For a fixed value of ϵ, $\Omega^2/\pi G\overline{\rho}$ increases with an increase in $\delta\rho/\rho_0$. As we have explained for the case of the double-layered spheroids (see Section 2.5), this tendency can be explained as follows: as the degree of central condensation of mass increases under the constant mean density $\overline{\rho}$, the surface gravity at the equator becomes larger (owing to the non-spherical mass distribution) and, as a result, the stronger centrifugal force, *i.e.*, the higher angular velocity Ω, is needed to maintain the same coaspect ratio of the equilibrium figure. As seen from this figure, ϵ_c seems to decrease with increasing $\delta\rho/\rho_0$. The detail of the behavior of ϵ_c on $\delta\rho/\rho_0$ and V_1/V_0 will be presented in Section 4.4.

The rotational angular momentum L at the equilibrium is shown in Fig. 4.12 for various values of the parameters ϵ and $\delta\rho/\rho_0$. Again, the volume ratio V_1/V_0 is taken to be 1/8. The definition of normalization constant is as same as that used in Chapter 2 for the double-layered spheroids. That is

$$\widetilde{L} = \frac{L}{(GM^3\,\overline{a})^{1/2}} \quad , \tag{4.3}$$

where M is the total mass of the body and $\overline{a}$ is the radius of the sphere which has a mass M and a mean density $\overline{\rho}$. This unit is equal to the angular momentum of a grazing satellite with mass M orbiting circularly around the body. Unlike the case of the angular velocity, for a fixed value of ϵ the normalized angular momentum $\widetilde{L}$ decreases with increasing $\delta\rho/\rho_0$ but the difference is very small. This comes from the fact that the decrease in the moment of inertia due to the mass concentration almost cancels out the increase in the angular velocity as long as $\delta\rho/\rho_0$ is relatively small.

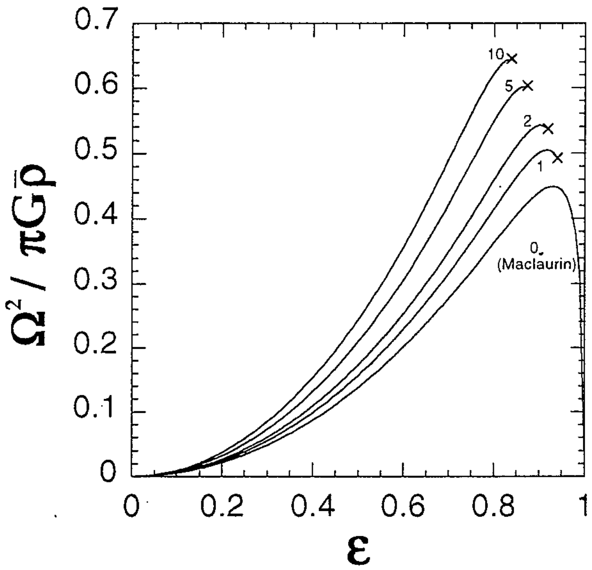

Fig. 4.11. The variation of the square of the angular velocity Ω against the coaspect ratio ϵ for various values of $\delta\rho/\rho_0$. The value of V_1/V_0 is taken to be 1/8. The curves are terminated at the critical coaspect ratio ϵ_c which are indicated by the cross "×". The curve attached by 0 corresponds to the Maclaurin spheroid.

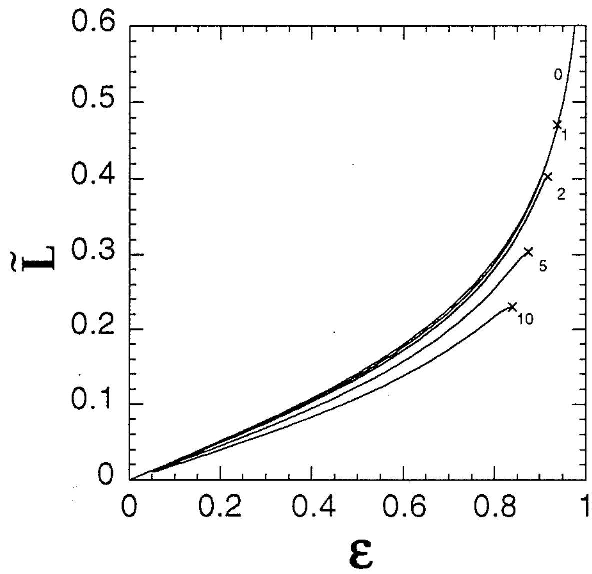

Fig. 4.12. The normalized angular momentum $\widetilde{L}$ against the coaspect ratio ϵ for various values of $\delta\rho/\rho_0$. The value of V_1/V_0 is taken to be 1/8 (as for the normalization, see text). The curves are terminated at the critical coaspect ratio ϵ_c which are indicated by the cross "×". The curve attached by 0 corresponds to the Maclaurin spheroid.

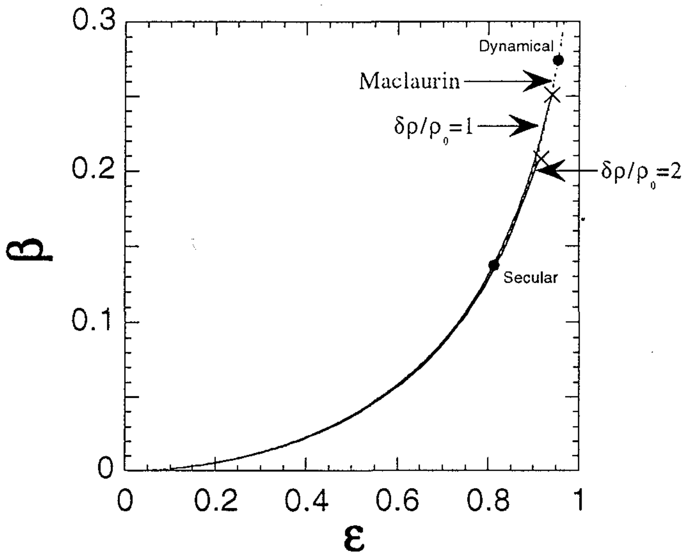

Fig. 4.13. The ratio of the rotational kinetic energy to the magnitude of the gravitational gravitational energy, β, against the coaspect ratio ϵ.

Next, let us consider a parameter β which is given by

$$\beta = \frac{T}{|W|} \quad , \tag{4.4}$$

where W is the gravitational energy defined by

$$W = \frac{1}{2}\int d\mathbf{x}\ \rho(r,\mu)\ \Phi_g(r,\mu) \tag{4.5}$$

and T is the total rotational kinetic energy given by

$$T = \frac{1}{2} I\ \Omega^2 \tag{4.6}$$

with the scalar moment of inertia I. The parameter β is often used as an index to quantify the points where the instability of the body sets in (Boss and Peale, 1986 ; Durisen and Gingold, 1986). In Fig. 4.13, β is shown as a function of ϵ. The solid curve denotes the $\beta - \epsilon$ relation of the Maclaurin spheroid. The points where the Maclaurin spheroid becomes dynamically and secularly unstable are also shown by the solid circles in Fig. 4.13. From this figure we can see that there is no apparent difference in β between the cases of the two-layered rotating body and of the Maclaurin spheroid. Thus, it is natural to expect that the value of ϵ where the secular instability occurs is almost the same as that of the Maclaurin spheroid. Moreover, we should keep in mind a possibility that the equilibrium figure reaches the critical coaspect ratio before the onset of dynamical instability. Onset of the instability will be described in detail in Chapter 5.

4.4. The critical coaspect ratio for the general cases

In Section 4.1, we mentioned the existence of the critical coaspect ratio only for the case where $V_1/V_0 = 1/8$ and $\delta\rho/\rho_0 = 1$. In this section, we will try to find the critical coaspect ratio ϵ_c more generally, namely, for the cases of the various values of V_1/V_0 and $\delta\rho/\rho_0$.

Let us first consider the limit of $\delta\rho/\rho_0 \to 0$. This corresponds to the case where there is no core in the body, *i.e.*, to the case of the Maclaurin spheroid. For the Maclaurin spheroids with density ρ_0 and the unit equatorial radius (*i.e.*, $a_1 = 1$), the total potential at the equatorial plane is given by (see Eqs. (2.32) to (2.36))

$$\frac{\Phi_t(x_1, 0)}{\pi G \rho_0} = A_1(e_0)x_1^2 - \left(2A_1(e_0) + (1-e_0^2)A_3(e_0)\right) + \frac{x_1^2}{2}\frac{\Omega^2}{\pi G\rho_0} \tag{4.7}$$

where e_0 is the eccentricity of the spheroid and $A_1(e_0)$ and $A_3(e_0)$ are the index symbols defined by Eqs. (2.17) and (2.18), respectively, in Section 2.2. Noting that ϵ_c is determined by the condition (see Section 4.2)

$$d\Phi_t/dx_1 = 0 \qquad \text{at } (x_1,\, x_3) = (1,\, 0) \quad , \tag{4.8}$$

We differentiate Eq. (4.7) with respect to x_1 and find

$$\begin{aligned} \frac{1}{\pi G\rho_0}\frac{d\Phi_t t}{dx_1} &= 2A_1(e_0)x_1 + \frac{\Omega^2}{\pi G\rho_0}x_1 \\ &= \frac{4\sqrt{1-e_0^2}}{e_0^2}\left[\left(2-e_0^2\right)\frac{\sin^{-1}e_0}{e_0} - 2\sqrt{1-e_0^2}\right]x_1 \quad , \end{aligned} \tag{4.9}$$

where we used Eqs. (2.17) (*i.e.*, definition of $A_1(e_0)$) and (2.41) (Maclaurin's formula). Since the function of e_0 enclosed by brackets is always positive in the range where $0 < e_0 < 1$, the

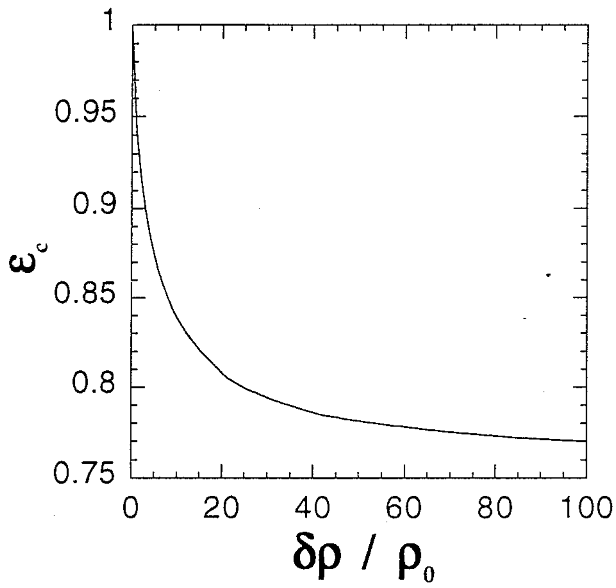

Fig. 4.14. The critical coaspect ratio ϵ_c as a function of the values of $\delta\rho/\rho_0$. The value of V_1/V_0 is taken to be 1/8.

right hand of Eq. (4.9) is always positive except the limit of $e_0 \to 1$. Therefore, the limit of $\delta\rho/\rho_0 \to 0$ we have

$$\epsilon_c \to 1 \quad . \tag{4.10}$$

Similarly, in the limit of $V_1/V_0 \to 0$ as well as the limit of $V_1/V_0 \to 1$, we can find the same result since the body becomes homogeneous in such limits.

Using criterion (4.8), we will find numerically the critical value ϵ_c for various parameters V_1/V_0 and $\delta\rho/\rho_0$ (note that the numerical accuracy of ϵ_c is of the order of 0.01). In Fig. 4.14, the relation between ϵ_c and $\delta\rho/\rho_0$ is shown in the case of $V_1/V_0 = 1/8$. The value of ϵ_c decreases as $\delta\rho/\rho_0$ increases. But it seems that there exists a minimum value in ϵ_c in the limit of $\delta\rho/\rho_0 \to \infty$. This tendency can be found for other values of V_1/V_0. The detail of the minimum value of ϵ_c will be considered at the end of this section. We also illustrate the relation between ϵ_c and V_1/V_0 in Fig. 4.15. The value of ϵ_c becomes lowest at the intermediate value of V_1/V_0. This is a reasonable result since the bodies with $V_1/V_0 \ll 1$ and $V_1/V_0 \sim 1$ correspond to the Maclaurin spheroid.

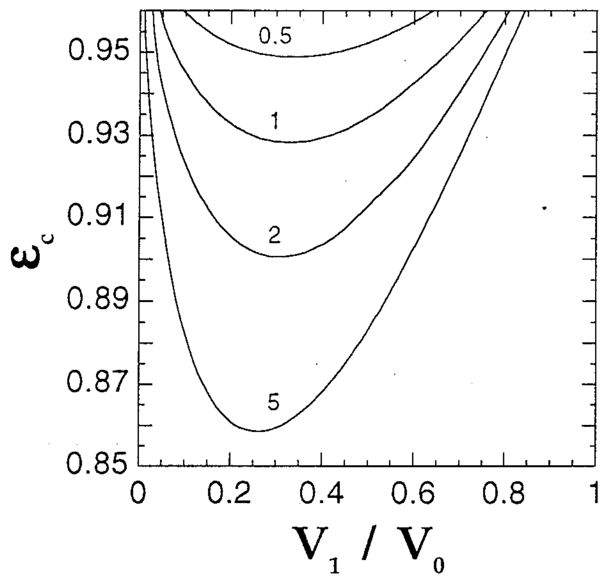

Fig. 4.15. The critical coaspect ratio ϵ_c as a function of the values of V_1/V_0. The curves are attached by the values of $\delta\rho/\rho_0$.

If the density of the core is much larger than that of the mantle, *i.e.*, $\delta\rho/\rho_0 \gg 1$, the body can be regarded as the "core" with density $\delta\rho$ surrounded by an "atmosphere" with very low density, ρ_0. In this case, the gravitational potential is governed only by the "core" and the figure of the "core" is regarded to be a Maclaurin spheroid. The figure of the "atmosphere" with the critical coaspect ratio ϵ_c can be determined by the following two conditions:

(1) The surface of the "atmosphere"" reaches the neutral point on the equatorial plane.

(2) The total potential Φ_t is constant throughout the surface.

In this case, the ellipsoidal coordinate λ at the point (x_1, 0, 0) outside the core is equal to x_1^2 - $a_1'^2$ (see Eq. (2.38)) and the total potential $\Phi_t(x_1, 0, 0)$ at that point is given by (see Eq. (2.37))

$$\begin{aligned}\Phi_t(x_1,0,0) &= -\frac{1}{2}\,\Omega^2\,x_1^2 \\ &+ \pi G\,\delta\rho\,\sqrt{1-e_1^2}\left\{\frac{2}{e_1}\left(1-\frac{x_1^2}{2a_1'^2e_1^2}\right)\sin^{-1}\frac{a_1'e_1}{x_1}+\frac{\sqrt{x_1^2-a_1'^2e_1^2}}{a_1'e_1^2}\right\}\quad, \qquad (4.11)\end{aligned}$$

where a_1' and e_1 are the equatorial radius and the eccentricity of the "core". Differentiating this equation with respect to x_1 and demanding $\partial\Phi_t/\partial x_1 = 0$, we obtain

$$
\begin{aligned}
-\,\Omega^2\,x_1 \;+\; \pi\,G\,\delta\rho\,\sqrt{1-e_1^2}\,\Bigg\{ & \frac{x_1}{a_1' e_1^2 \sqrt{x_1^2 - a_1'^2 e_1^2}} \\
& - \frac{2a_1'\left(1 - x_1^2/2a_1'^2 e_1^2\right)}{x_1^2\sqrt{1 - a_1'^2 e_1^2/x_1^2}} - \frac{2x_1 \sin^{-1}\left(a_1' e_1/x_1\right)}{a_1'^2 e_1^3} \Bigg\} = 0 \;.
\end{aligned}
\tag{4.12}
$$

This is a non-linear equation giving the x_1-coordinate of the neutral point. Unlike other parts of this paper, here the equatorial radius of the "core" is taken to be 1. Noting that Ω^2 is determined by the Maclaurin's formula (see Eq. (2.41))

$$
\frac{\Omega^2}{\pi G \delta\rho} = \frac{2\sqrt{1-e_1^2}}{e_1^3}\left(3 - 2e_1^2\right)\sin^{-1} e_1 - \frac{6}{e_1^2}\left(1 - e_1^2\right) \quad , \tag{4.13}
$$

we can find the equatorial radius of the "atmosphere", x_1, by the use of the Newton-Raphson method for an arbitrary value of the eccentricity of the "core", e_1. After that, we readily draw the equi-potential surface, *i.e.*, the surface of the "atmosphere", which passes through the neutral point. Thus, the volume ratio V_1/V_0 and ϵ_c can be calculated.

An example of the solution in the case where $e_1 = 0.4$ is shown in Fig. 4.16. Repeating this procedure for various e_1, we obtain the relation between ϵ_c and the volume ratio in the limit of $\delta\rho/\rho_0 \to \infty$. The results are shown in Fig. 4.17. From this figure, the limiting value of ϵ for the case where $V_1/V_0 = 1/8$ is found to be

$$
\epsilon \to 0.756 \quad . \tag{4.14}
$$

The curve in Fig. 4.14 seems to focus this limiting value.

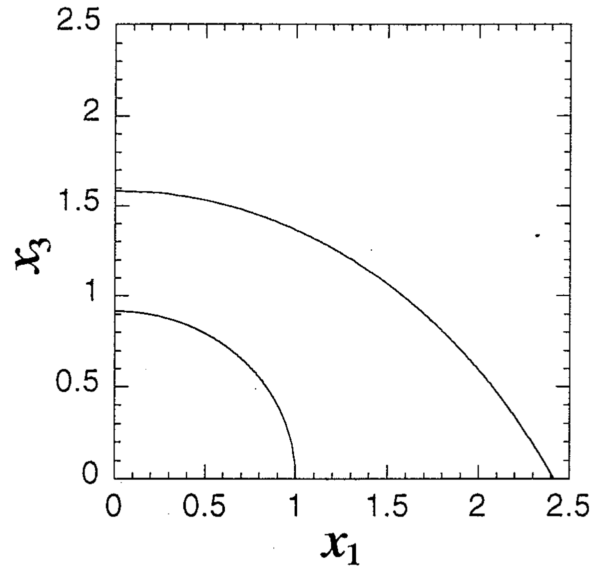

Fig. 4.16. The meridional cross section in the limit of $\delta\rho/\rho_0 \to \infty$. The eccentricity of the core e_1 is taken to be 0.4. In this case, the volume ratio V_1/V_0 and the coaspect ratio of the body surface ϵ are equal to 0.12151 and 0.755, respectively.

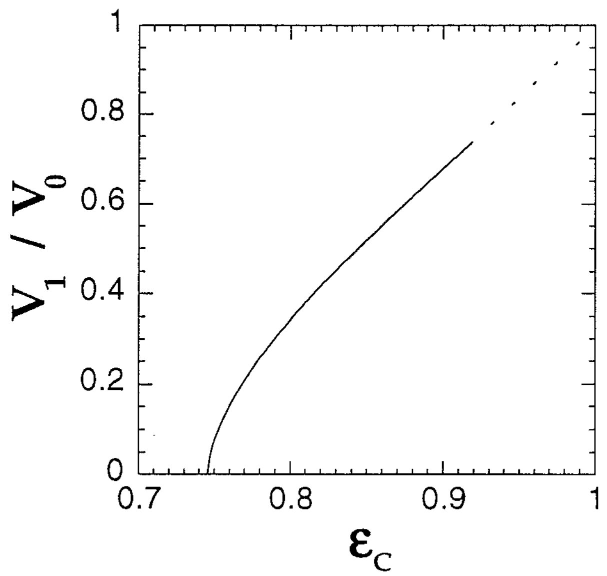

Fig. 4.17. The critical coaspect ratio ϵ_c against the volume ratio V_1/V_0 in the limit of $\delta\rho/\rho_0 \to \infty$.

5. Stability of the Equilibrium Figure

5.1. Criterion for stability

In order to investigate the stability of the two-layered incompressible, rotating bodies, we will adopt the stability criterion which was first derived by Chandrasekhar and Lebovitz (1962). They investigated the stability of the rotating gaseous masses against small perturbations using the tensor formalism of the second order virial theorem and found the critical angular velocity at which the secular and dynamical instabilities set in. Details of derivation of this criterion is reviewed in Appendix.

Suppose a mass element located at $\mathbf{x}$ in a unperturbed state is displaced slightly to $\mathbf{x} + \xi$. Then we assume that the displacement $\xi = (\xi_1, \xi_2, \xi_3)$ can be represented by the form of

$$d\xi_i = X_{ik}\, x_k e^{i\sigma t} \quad , \tag{5.1}$$

where X_{ik} are constants and σ is the frequency of the perturbation. If the characteristic root σ is zero, then the figure is neutral against such perturbations. This corresponds to the secular instability. Moreover, if the characteristic root σ becomes complex, then the amplitude of the perturbation grows with time and, hence, the figure becomes unstable. This corresponds to the dynamical instability.

According to Chandrasekhar and Lebovitz (1962), we will restrict ourselves to the case where the displacement vector is given by

$$\begin{cases} \xi_1 &= \{X_{11}x_1 \;+\; X_{12}x_2\}\; e^{-i\sigma t} \,, \\ \xi_2 &= \{-X_{11}x_2 \;+\; X_{12}x_1\}\; e^{-i\sigma t} \,, \\ \xi_3 &= 0 \,. \end{cases} \tag{5.2}$$

This mode corresponds the deformation that elongates or shortens the spheroid in the horizontal direction, or, in other words, transforms the spheroid into a triaxial ellipsoid. Assuming Eq.

(5.2), Chandrasekhar and Lebovitz (1962) found that when the condition

$$\Omega^2 = W_{12,12}/I_{11} \tag{5.3}$$

is satisfied, then the characteristic root σ becomes zero. In the above, $W_{ij;kl}$ is a super-matrix defined by

$$W_{ij;kl} = \int_V \rho x_i \frac{\partial U_{ij}}{\partial x_l} d\mathbf{x} \tag{5.4}$$

where

$$\frac{U_{ij}}{\pi G \rho_0} = \int_{V_0} \frac{(x_i - x_i')(x_j - x_j')}{|\mathbf{x} - \mathbf{x}'|^3} d\mathbf{x}' \quad . \tag{5.5}$$

For a homogeneous spheroid (*i.e.*, the Maclaurin spheroid), Eq. (5.3) is exactly satisfied at $e_0 = 0.81267$, *i.e.*, the point where the secular instability sets in, in other words, for the Maclaurin spheroids, Eq. (5.3) gives the exact point where the Maclaurin sequence (a sequence of spheroids) bifurcates to the Jacobi sequence (a sequence of triaxial spheroids).

Furthermore, when the condition

$$\Omega^2 I_{11} < 2 W_{12;12} \tag{5.6}$$

is satisfied, then σ becomes complex and the amplitude of the perturbation grows with time. In such a case, the figure is unstable against linear oscillations. It can be readily shown that, for the Maclaurin spheroids, Eq. (5.6) also coincides exactly with the condition of the dynamical instability.

The stability analysis mentioned above is not complete since the mode of perturbation is artificially limited in the form of Eqs. (5.1) and (5.2), In fact, as Tassoul (1978) pointed out that the condition (5.3) is merely an approximate one for the case of centrally condensed bodies and found that the bifurcation to triaxial figure may occur when Ω^2 is less than $W_{12;12}/I_{11}$. So, it would be safe to regard that the condition (5.3) is a *sufficient condition* for the onset of the secular instability for centrally condensed bodies. However, we can expect that the above-mentioned method of the stability analysis gives the criterion, at least approximately, since the degree of the central condensation of mass is relatively small (compare the gaseous gravitating body where the central density is as, for example, 50 times as the mean density). So we will apply the method of Chandrasekhar and Lebovitz to our present stability analysis.

5.2. Evaluation of super-matrix $W_{12;12}$

In the present study, we assume that the body has a symmetry not only about its rotational axis but also about its equatorial plane. Then, the super-matrix $W_{12;12}$ defined by Eq. (5.4) can be rewritten, using the cylindrical coordinates (ϖ, φ, z), as

$$W_{12;12} = \frac{\pi}{4} \int\int \rho(\varpi, z)\ D_\varpi \left[\varpi^4 D_\varpi \left(D_\varpi\, \chi(\mathbf{x})\right)\right]\ \varpi\ d\varpi dz \quad , \tag{5.7}$$

where $\chi(\mathbf{x})$ is the super potential of the gravitational field defined by

$$\chi(\mathbf{x}) = -G \int_V \rho(x)\ |\mathbf{x} - \mathbf{x}'|\ d\mathbf{x}' \tag{5.8}$$

and D_ϖ is the operator defined by

$$D_\varpi = \frac{1}{\varpi} \frac{\partial}{\partial \varpi} \tag{5.9}$$

(Tassoul and Ostriker, 1968). Making use of the results of Chandrasekhar and Lebovitz (1962), we can write

$$D_\varpi\, \chi(\mathbf{x}) = -\Phi_g(\mathbf{x}) + \frac{G}{\varpi} D(\mathbf{x}) \tag{5.10}$$

where $\Phi_g(\mathbf{x})$ denotes the gravitational potential

$$\Phi_g(\mathbf{x}) = -G \int d\mathbf{x}'\ \frac{\rho(r, \mu)}{|\mathbf{x} - \mathbf{x}'|} \tag{5.11}$$

and $D(\mathbf{x})$ is the potential function defined by

$$D(\mathbf{x}) = \int_V \rho(\mathbf{x}')\ \frac{\varpi' \cos(\varphi - \varphi')}{|\mathbf{x} - \mathbf{x}'|}\ d\mathbf{x}' \quad . \tag{5.12}$$

In order to evaluate the potential function $D(\mathbf{x})$, we expand $|\mathbf{x} - \mathbf{x}'|^{-1}$ in a series of the Legendre polynomials $P_n(\cos\alpha)$ where α is the angle between two position vectors $\mathbf{x}$ and $\mathbf{x}'$.

Furthermore, applying the well-known sum rule in terms of the Legendre associated function P_n^m, we have,

$$|\mathbf{x}-\mathbf{x}'|^{-1} = \frac{1}{r_>}\sum_{n=0}^{\infty}\left(\frac{r_<}{r_>}\right)^n P_n(\cos\alpha)$$

$$= \frac{1}{r_>}\sum_{n=0}^{\infty}\left(\frac{r_<}{r_>}\right)^n \left[P_n(\mu)\,P_n(\mu') + 2\sum_{m=1}^{n}\frac{(n-m)!}{(n+m)!}P_n^m(\mu)\,P_n^m(\mu')\cos m(\varphi-\varphi')\right] \tag{5.13}$$

where the larger and the smaller lengths of $\mathbf{x}$ and $\mathbf{x}'$ are denoted by $r_>$ and $r_<$, respectively. Furthermore, we use here the spherical coordinates $(r,\ \theta,\ \varphi)$ together with $\mu = \cos\theta$ and $\mu = \cos\theta'$. Inserting this expression into Eq. (5.12) and integrating over φ', we find that the first term in the bracket as well as the terms in the summation except for $m = 1$ vanish and obtain

$$D(\mathbf{x}) = 4\,\pi\,G\sum_{k=0}^{\infty}\frac{P_{2k+1}^1(\mu)}{(2k+1)(4k+3)}\int_0^1 d\mu'\,\rho(\varpi,z)\ f(r,\mu;k)\left\{P_{2k+1}^1(\mu') - P_1^1(\mu')\right\}\ , \tag{5.14}$$

where $f(r,\mu;k)$ is a function defined by

$$f(r,\mu;k) = \begin{cases} \left(\frac{1}{2k+5} + \frac{1}{2k-2}\right)r^3 - \frac{1}{2k-2}\frac{r^{2k+1}}{R(\mu)^{2k-2}}\ , & \text{for } r < R \text{ and } n \neq 1, \\ \frac{r^3}{7} + r^3\ (\log R(\mu) - \log r)\ , & \text{for } r < R \text{ and } n = 1, \\ \frac{1}{r^{2k+5}}\frac{R(\mu)^{2k+5}}{2k+5}\ , & \text{for } r \geq R\ . \end{cases} \tag{5.15}$$

Note that the even order terms in the summation in Eq. (5.13) is eliminated because of the assumption of the symmetry about the equatorial plane. Since the product of the Legendre associated function $P_n^1\ P_1^1$ can be written in terms of the Legendre polynomials as

$$P_n^1(\mu)\,P_n^1(\mu) = \frac{n\,(n+1)}{2n+1}\ \{P_{n-1}(\mu) - P_{n+1}(\mu)\}\ , \tag{5.16}$$

we can rewrite Eq. (5.13) into the following form

$$D(\mathbf{x}) = 4\,\pi\,G\sum_{k=0}^{\infty}\frac{P_{2k+1}^1(\mu)}{4k+3}\int_0^1 d\mu'\ f(r,\mu';k)\ \rho(\varpi,z)\ \{P_{2k}(\mu') - P_{2k+2}(\mu')\}\ . \tag{5.17}$$

The expanded form of Φ_g is given by Eq.(3.4). Noting the definition of the operator D_ϖ, we find as the desired expression of $W_{12;12}$ in cylindrical coordinates

$$W_{12;12} = \int_0^{z_0}\int_0^{\varpi_0}\left\{-D + \varpi\frac{\partial D}{\partial\varpi} - 3\varpi^2\frac{\partial\Phi_g}{\partial\varpi} + \varpi^2\frac{\partial^2 D}{\partial\varpi^2} - \varpi^3\frac{\partial^2\Phi_g}{\partial\varpi^2}\right\}d\varpi dz\ , \tag{5.18}$$

where subscript "0" indicates the value at the boundary.

5.3. Numerical results

In order to evaluate the double integral (5.18), we have to know the potentials $\Phi_g(\mathbf{x})$ and $D(\mathbf{x})$ and their derivatives with respect to ϖ at an arbitrary internal point of the body. As we evaluated the gravitational potential $\Phi_g(\mathbf{x})$ (see Section 3.2), the potential function $D(\mathbf{x})$ is described as a sum of the potential function D_0 and D_1: the former is due to the body with density ρ_0 and volume V_0 and the latter is due to the body with density $\delta\rho$ and volume V_1.

To calculate the value of the potentials $\Phi_g(\mathbf{x})$ and $D(\mathbf{x})$, we divide the meridional cross section of the equilibrium figure into a number of rectangular grids. In the x_3-direction, we divide the region with a constant interval. To minimize the error of calculated potential, we subdivide the grid near the pole where $x_3 > 0.8a_3$ (a_3 being the semimajor axis of the pole). In the x_1-direction, we divide the region with a constant interval (but depends on x_3). The number of the grids are taken to be 100×100.

The potentials Φ_g and D at the grid point are calculated using spherical coordinates (see Eqs. (3.13), (3.14), and (5.17)). The Legendre polynomials and the Legendre associated polynomials used in the calculation of the potential are taken up to the rank of 40 and 39, respectively. We made use of Newton's differentiation formula for the evaluation of derivatives with respect to ϖ at grid points and Simpson's method for the numerical integrations over μ, ϖ, and z.

In order to check the accuracy of our method, using the super-matrix $W_{12;12}$ and the moment of inertia tensor I_{11} obtained numerically for the homogeneous spheroid ($V_1/V_0 = 1$) with $\epsilon_0 = 0.81267$, *i.e.*, the critical eccentricity of the onset of the secular instability for the Maclaurin spheroid, we calculate the ratio of $W_{12;12}$ to $\Omega^2\ I_{11}$ (Ω^2 is evaluated from Maclaurin's formula) which is to be equal to 1. The relative error between the numerical values and analytical values of the potential Φ_g and D is, at most, about 0.001 %. The relative error of the derivatives of the potential Φ_g and D with respect to ϖ is, at most, about 0.01 %. At $e_0 = 0.81267$ where the secular instability sets in for the Maclaurin spheroid , the criterion (5.3) must be satisfied. In our numerical calculation, the difference between them is about 0.1 %. Similarly, at $e_0 = 0.9512$

where the dynamical instability sets in for the Maclaurin spheroid, the criterion (5.6) must be satisfied. In our calculation, the difference between them is about 0.1 %, too. Therefore, we can expect that by our numerical method mentioned above we can determine the critical point of the onset of the instability within the accuracy of about 0.1 %.

In Fig. 5.1 we show the variation of the ratio of the super-matrix $W_{12;12}$ to $\Omega^2\ I_{11}$ against the coaspect ratio ϵ in the case where $\delta\rho/\rho_0 = 1$ and $V_1/V_0 = 1/8$. The curve is terminated at the point (marked by the cross $\times$) where ϵ is equal to the critical coaspect ratio ϵ_c described in the previous chapter. The dashed horizontal line denotes the position where the criterion of the secular instability (Eq. (5.3)) is satisfied. From Fig. 5.1, we find that solid curve intersect with the dashed curve at the point where

$$\epsilon_s \sim 0.812 \quad . \tag{5.19}$$

In the above, subscript 's' denotes the secular instability. This value almost coincides with that of the Maclaurin spheroid $\epsilon_s = 0.81267$ within the accuracy of our calculation. The dotted horizontal line denotes the position where the criterion of the dynamical instability (Eq. (5.6)) is satisfied. We should note that the curve terminates before crossing the dotted line. This means that the dynamical instability does not occur. Instead, as Boss (1986) pointed out, when the coaspect ratio exceeds the critical value ϵ_c, mass shedding from the equatorial plane may begin.

Let us next see the effect of the density contrast $\delta\rho/\rho_0$ on ϵ_s. The ratio of super-matrix $W_{12;12}$ to $\Omega^2\ I_{11}$ is shown in Fig. 5.2 as a function of the coaspect ratio ϵ in the case where $\delta\rho/\rho_0 = 2$ and $V_1/V_0 = 1/8$. The physical meanings of the dashed and dotted horizontal lines are the same as Fig. 5.1. As seen from this figure, the solid curve and the dashed line never intersect as in the case of $\delta\rho/\rho_0 = 1$. Thus, the dynamical instability does not occur in this case, too. This feature is true for larger values of $\delta\rho/\rho_0$. The point where the criterion for the secular instability (Eq. (5.3)) is satisfied when

$$\epsilon_s \sim 0.817 \quad . \tag{5.20}$$

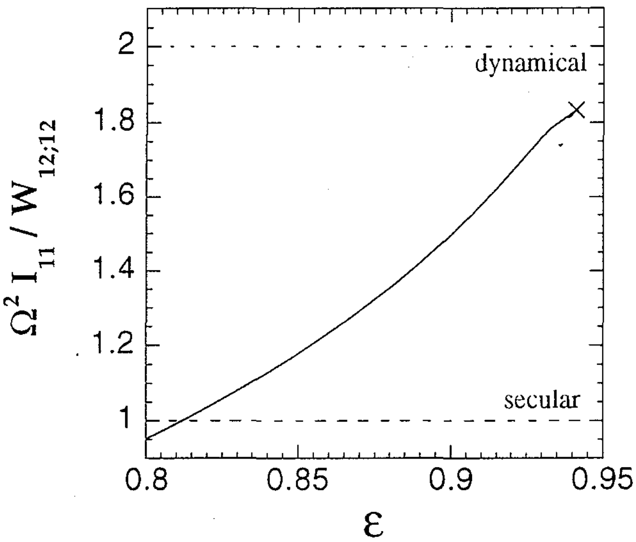

Fig. 5.1. The variations of the ratio $W_{12;12}/\Omega^2\ I_{11}$ against the coaspect ratio ϵ. The values of $\delta\rho/\rho_0$ and V_1/V_0 are taken to be 1 and 1/8, respectively. The symbol "×" corresponds to the critical aspect ratio. The dashed and dotted horizontal lines denote, respectively, the positions where the secular instability and the dynamical instability begin.

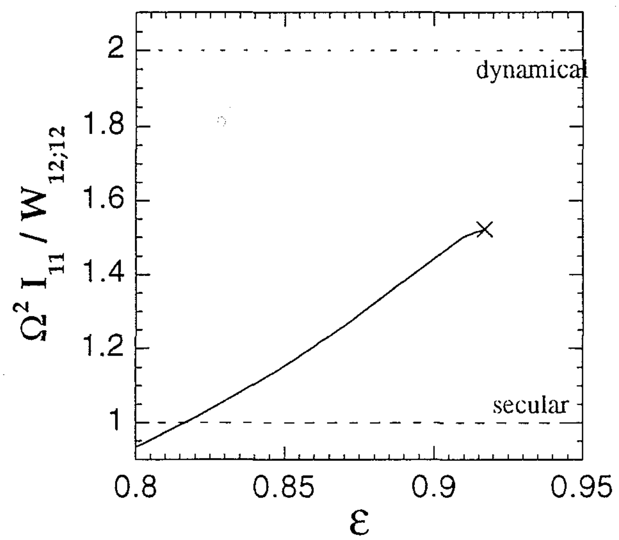

Fig. 5.2. The same as Fig. 5.1 but for the case where $\delta\rho/\rho_0 = 2$.

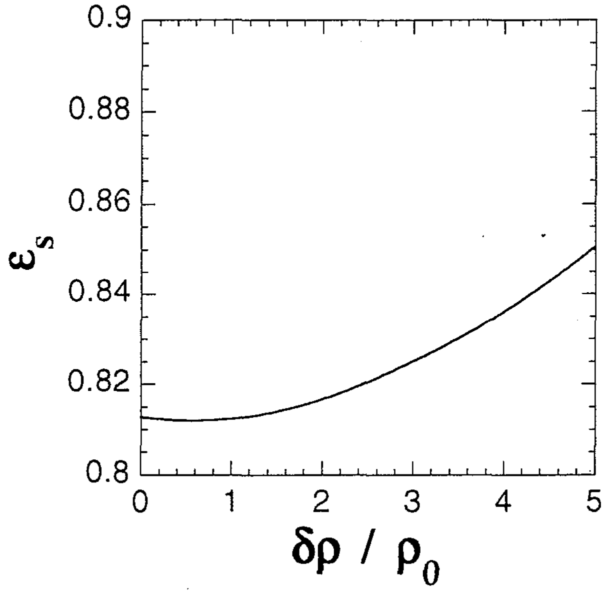

Fig. 5.3. The coaspect ratio where the secular instability sets in for various density ratios $\delta\rho/\rho_0$. The volume ratio V_1/V_0 is taken to be 1/8. The case where $\delta\rho/\rho_0 = 0$ corresponds to the Maclaurin spheroid.

We illustrate the variation of ϵ_s against $\delta\rho/\rho_0$ in Fig. 5.3. The value of ϵ_s increases slightly and almost monotonically with $\delta\rho/\rho_0$. In other words, as the degree of central condensation of mass increases the body becomes more stable against the perturbations.

Finally, let us see the effect of the volume ratio V_1/V_0 on the criterion of the instability. To save the computational time, the numerical calculations are only executed for $V_1/V_0 = 1/8$, 1/3, 1/2, and 2/3. The results are summarized in Table. 5.1 for the case of $\delta\rho/\rho_0 = 1$. We can see from the table that the point where the criterion for the secular instability sets in does not strongly depends on the volume ratio V_1/V_0. It should be noted that, in all of four cases, the equilibrium figures reach to the critical coaspect ratio before the condition for dynamical instability is satisfied. However, as seen from the Fig. 4.14, in the limit of $V_1/V_0 \to 1$ and 0, we can expect that the dynamical instability occurs before reaching critical coaspect ratio.

Therefore, the condition for the secular instability is not eased compared to the Maclaurin

Table 5.1. The coaspect ratio where the secular instability sets in for various volume ratios V_1/V_0. The volume ratio $\delta\rho/\rho_0$ is taken to be 1. For the cases where $V_1/V_0 = 0$ and 1, the bodies become homogeneous spheroids, *i.e.*, Maclaurin spheroid.

V_1 / V_0	ε_s
0 (Maclaurin)	0.81267
1/8	0.812
1/3	0.816
1/2	0.816
2/3	0.815
1 (Maclaurin)	0.81267

spheroid even if the inhomogeneity of the body is taken into account. Moreover, this condition does not strongly depends on the values of the parameters, V_1/V_0 and $\delta\rho/\rho_0$. For all cases we calculated here, the body reaches to the critical coaspect ratio ϵ_c before the dynamical instability sets in.

6. Conclusion and Discussion

We have studied the equilibrium figures and their stabilities of self-gravitating, rotating, and axis-symmetric body composed of two-layered incompressible fluids. Our results are summarized as follows:

(1) When the rotation is slow, both body surface and the core-mantle boundary are well approximated by spheroids.

(2) As the body rotates faster, the coaspect ratio $\epsilon = \sqrt{1 - a_3^2/a_1^2}$ increases, *i.e.*, the body surfaces is suppressed toward the equatorial plane. When the coaspect ratio ϵ exceeds 0.8 the body surface begins to deviate appreciably from a spheroid while the core-mantle boundary is still spheroidal.

(3) The coaspect ratio ϵ has an upper limit ϵ_c: if the coaspect ratio exceeds this upper limit, no equilibrium figure exists as a single and axis-symmetric body. The value of ϵ_c decreases with an increase in $\delta\rho/\rho_0$ and takes its minimum value at $V_1/V_0 \sim 1/3$.

(4) The condition for the secular instability is almost the same as that of the Maclaurin spheroid and it does not strongly depends on the values of the parameters, V_1/V_0 and $\delta\rho/\rho_0$. For the cases of $V_1/V_0 = 1/8$, $1/3$, $1/2$, and $2/3$, the body reaches to the critical coaspect ratio ϵ_c before the dynamical instability occurs.

Now, let us apply our results to the rotational fission hypothesis of the lunar origin. We first consider what the values $\delta\rho/\rho_0$ and V_1/V_0 are most suitable for the proto-Earth. The density distribution of the present Earth is shown in Fig. 6.1 (Ringwood, 1979). As a first approximation, both the core and the mantle may be regarded to be homogeneous and, hence, the Earth can be approximated as the two-layered rotating body composed of incompressible materials. The mean density of the mantle is about $\rho_{\rm mantle} \sim 4.51$ [g/cm^3] and the mean density

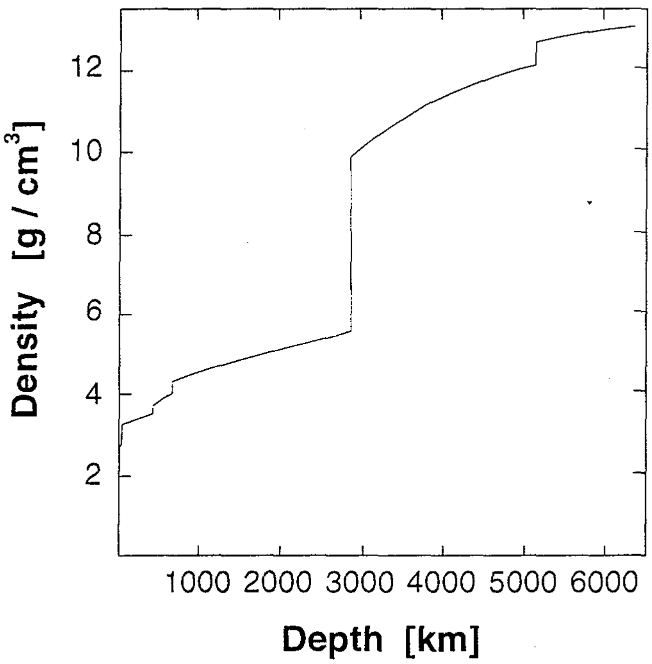

Fig. 6.1. The density distribution inside the present Earth (after Ringwood, 1979).

of the whole core is as large as 10.8 [g/cm^3]. Therefore, for the value of $\delta\rho/\rho_0$ of the present Earth we have

$$\delta\rho/\rho_0 \sim 1.39 \quad . \tag{6.1}$$

If we consider the proto-Earth which is in the process of the core formation, then, the core density would be smaller than that of the present Earth. In this sense, the above value of $\delta\rho/\rho_0$ is the upper limit. The ratio of the volume of the core to that of the present Earth V_1/V_0 is

$$\frac{V_1}{V_0} \sim 0.162 \quad . \tag{6.2}$$

Even if the volume torn from the magma ocean is taken into account, V_1/V_0 does not increase any more.

Thus, we can consider that for the proto-Earth $\delta\rho/\rho_0$ was in the range between 0 and 1.39 whereas V_1/V_0 was in the range between 0 and 0.162. As we have seen in the previous chapter, for these ranges of parameters ρ/ρ_0 and V_1/V_0, the dynamical instability never occurs. Instead,

Table 6.1. The angular momenta needed for the secular instability L_{secular} and for the mass-shedding L_{critical}. The values are normalized by the total angular momentum of the present Earth-Moon system.

$\delta\rho / \rho_0$	V_1 / V_0	L_{secular}	L_{critical}
1	1/8	2.596	4.087
1	1/3	2.563	3.647
1	1/2	2.561	3.734
1	2/3	2.581	4.103
2	1/8	2.569	3.507
2	1/3	2.509	3.056

mass shedding from the equator may possibly occur if the proto-Earth had a sufficiently large angular momentum. That is materials would be ejected from the equator to form a disk around the proto-Earth. Boss (1986) simulated numerically the highly rotating proto-Earth with polytropic density distribution of index 1/2 and observed that about 10 lunar masses are put into orbit.

The angular momenta needed for the secular instability and for mass-shedding (*i.e*, the system reaches the critical coaspect ratio) are tabulated in Table 6.1. As seen from this table, the magnitude of the angular momentum which is necessary to trigger the mass shedding is at least three times as large as that of the present Earth-Moon system. However, if we consider that the values of $\delta\rho/\rho_0$ and V_1/V_0 are within the ranges described above, the condition is almost the same as that of the dynamical instability of the Maclaurin spheroid. It seems very unlikely that the proto-Earth gained such a large amount of the angular momentum even if a planet-sized object collides with the proto-Earth. Moreover, whatever the proto-Earth gained enough angular momentum, the excess angular momentum must thrown away by ejecting some part of the debris outside the Earth-Moon system. Such a process is never known until now.

We thus conclude that the rotational fission for the lunar origin is unlikely even if the inhomogeneity of the proto-Earth is taken account. Therefore, if the Moon was formed from the materials of the terrestrial magma ocean, we must look for another mechanism to strip the magma ocean and put enough materials into the suitable orbits.

Acknowledgments

The author wishes to express his gratitude to Professor K. Nakazawa for his great deal of valuable advise, continuing encouragement, and critical reading of this manuscript. He thanks Assistant Professor S. Ida, Drs. H. Emori, H. Tanaka for fruitful discussions. He is also grateful to Mr. T. Okuchi for useful advise about the geochemical constraints on the lunar origin. Numerical calculations were performed by CRAY C916 supercomputer at the Computer Center of the Tokyo Institute of Technology.

Appendix Derivation of the Criterion for Stability

In this Appendix, we will review the derivation of the criterion for stability of the equilibrium figure against small oscillations which was developed by Chandrasekhar and Lebovitz (1962).

In a rotating frame, second order virial equation is given by

$$\begin{aligned} \frac{d}{dt}\int_V \rho x_i u_j d\mathbf{x} &= 2T_{ij} + W_{ij} + \delta_{ij}\int_V p d\mathbf{x} + \Omega^2 I_{ij} - I_{il}\Omega_l\Omega_j \\ &+2\int_V \rho x_i \epsilon_{jlm} u_l \Omega_m d\mathbf{x} \end{aligned} \tag{A.1}$$

where u_i denotes the velocity component due to the internal motion and ϵ_{jlm} is Eddington's epsilon (*i.e.*, the completely antisymmetric third rank tensor). Furthermore, T_{ij}, I_{ij}, and W_{ij} are the tensors defined, respectively, by

$$T_{ij} = \frac{1}{2}\int_V \rho u_i u_j d\mathbf{x} \tag{A.2}$$

$$I_{ij} = \int_V \rho x_i x_j d\mathbf{x} \quad , \tag{A.3}$$

and

$$W_{ij} = -\frac{1}{2}\, G \int_{\mathrm{V}} \rho(\mathbf{x}) \;\, U_{ij}(\mathbf{x}) \;\, d\mathbf{x} \quad , \tag{A.4}$$

with

$$U_{ij} = \int_{\mathrm{V}} \rho(\mathbf{x}) \frac{(x_i - x_i')\,(x_j - x_j')}{|\mathbf{x}-\mathbf{x}'|^3} d\mathbf{x}' \quad . \tag{A.5}$$

The tensors T_{ij}, I_{ij}, and W_{ij} are called, respectively, the kinetic energy tensor, the moment of inertia tensor, and the potential energy tensor. It should be noted, unlike previous chapters, we take summation over repeated indices 'l' and 'm'.

Suppose a mass element located at $\mathbf{x}$ in an unperturbed state is displaced slightly to $\mathbf{x} + \xi$. Then, the first variation of Eq. (A.1) is written by

$$\begin{aligned} \frac{d^2}{dt^2}\int_V \rho x_i \xi_j d\mathbf{x} = & -\int_V \rho \xi_i \frac{\partial U_{ij}}{\partial x_l} d\mathbf{x} + \delta_{ij}\int_V (1-\gamma) p \,\mathrm{div}\xi d\mathbf{x} \\ & +\Omega^2 \int_V \rho(x_i\xi_j + \xi_i x_j) d\mathbf{x} - \Omega_j\Omega_l \int_V \rho(x_l\xi_j + \xi_l x_j) d\mathbf{x} \\ & +\frac{d}{dt}\int_V \rho x_i \epsilon_{jlm}\xi_l\Omega_m d\mathbf{x} \quad , \end{aligned} \tag{A.6}$$

where γ denotes the ratio of the specific heat.

We assume that the component of the displacement can be written in the form

$$d\xi_i = X_{ik}\, x_k e^{i\sigma t} \quad , \tag{A.7}$$

where X_{ik} are constants and σ is the frequency of the perturbation. If the frequency σ is zero, then the figure is neutral against such perturbations. Furthermore, if the frequency σ becomes complex, then the amplitude of the perturbation grows with time and, hence, the equilibrium figure becomes unstable. Substituting Eq. (A.7) into Eq. (A.6) (the direction of x_3-axis is taken to be parallel to the rotational angular velocity vector), we have

$$\begin{aligned} -\sigma^2 X_{jl} I_{li} = \; & 2i\epsilon_{jl3} X_{lm} I_{mi} + \Omega^2 (X_{jl} I_{li} + X_{il} I_{lj}) \\ & -\Omega^2 \delta_{j3} (X_{3l} I_{li} + X_{il} I_{l3}) - X_{lm} W_{ml;ij} + J X_{mm} \delta_{ij} \end{aligned} \tag{A.8}$$

where $W_{ij;kl}$ is called the super-matrix which is defined by

$$W_{ij;kl} = \int_V \rho x_i \frac{\partial U_{ij}}{\partial x_l} d\mathbf{x} \tag{A.9}$$

and J is the thermodynamical energy defined by

$$J = \int_V (1-\gamma)\; p \; d\mathbf{x} \quad . \tag{A.10}$$

If the body is axisymmetric with respect to its rotational axis, nine components of Eq. (A.8) can be readily written down:

$$-\sigma^2 X_{11} I_{11} = 2i\sigma\Omega X_{21} I_{11} + 2\Omega^2 X_{11} I_{11} + J X_{ll} - (X_{11} W_{11;11} + X_{22} W_{22;11} + X_{33} W_{33;11}) \; , \tag{A.11}$$

$$-\sigma^2 X_{22} I_{11} = -2i\sigma\Omega X_{12} I_{11} + 2\Omega^2 X_{22} I_{11} + J X_{ll} - (X_{11} W_{22;11} + X_{22} W_{11;11} + X_{33} W_{33;11}) \; , \tag{A.12}$$

$$-\sigma^2 X_{33} I_{33} = J X_{ll} - (X_{11} + X_{22})\, W_{33;11} - X_{33} W_{33;33} \; , \tag{A.13}$$

$$-\sigma^2 X_{21} I_{11} = -2i\sigma\Omega X_{11} I_{11} + \left(\Omega^2 I_{11} - W_{12;12}\right)(X_{21} + X_{12}) \; , \tag{A.14}$$

$$-\sigma^2 X_{12} I_{11} = 2i\sigma\Omega X_{22} I_{11} + \left(\Omega^2 I_{11} - W_{12;12}\right)(X_{12} + X_{21}) \; , \tag{A.15}$$

$$-\sigma^2 X_{31} I_{11} = -X_{13} W_{31;13} - X_{31} W_{13;13} \; , \tag{A.16}$$

$$-\sigma^2 X_{32} I_{11} = -X_{23} W_{31;13} - X_{32} W_{13;13} , \tag{A.17}$$

$$-\sigma^2 X_{13} I_{33} = 2i\sigma\Omega X_{23} I_{33} + \left(\Omega^2 I_{33} - W_{31;13}\right) X_{13} + \left(\Omega^2 I_{33} - W_{13;13}\right) X_{31} , \tag{A.18}$$

and

$$-\sigma^2 X_{23} I_{33} = 2i\sigma\Omega X_{13} I_{33} + \left(\Omega^2 I_{33} - W_{31;13}\right) X_{23} + \left(\Omega^2 I_{33} - W_{13;13}\right) X_{32} . \tag{A.19}$$

Since Eqs. (A.11) to (A.19) are independent each other, there are nine independent modes of perturbation. Among them, according to Chandrasekhar and Lebovitz (1962), we restrict ourselves to the mode where only X_{11}, X_{12}, X_{21}, and X_{22} are finite and remaining X_{ij}'s are zero. If we put another restriction on the displacements that they have to preserve the whole volume of the equilibrium figure, then the four remaining constants X_{ij} cannot be independent:

$$X_{11} = -X_{22} \quad \text{and} \quad X_{12} = X_{21} . \tag{A.20}$$

Therefore, the displacement vector is given by

$$\begin{cases} \xi_1 &= \{X_{11} x_1 + X_{12} x_2\} \; e^{-i\sigma t} , \\ \xi_2 &= \{-X_{11} x_2 + X_{12} x_1\} \; e^{-i\sigma t} , \\ \xi_3 &= 0 . \end{cases} \tag{A.21}$$

This mode corresponds the deformation that elongates or shortens the spheroid in the horizontal direction, or, in other words, transforms the spheroid into a triaxial ellipsoid. Chandrasekhar and Lebovitz showed that the axisymmetric figure is stable against other six modes of perturbation. Subtracting Eq. (A.12) from Eq. (A.11), we have

$$\begin{aligned} -\sigma^2 I_{11} (X_{11} - X_{22}) = \; & 2i\sigma\Omega X_{21} (X_{21} - X_{12}) + 2\Omega^2 I_{11} (X_{11} - X_{22}) \\ & - (W_{11;11} - W_{22;11}) (X_{11} - X_{22}) . \end{aligned} \tag{A.22}$$

With the help of the relation between the components of the super-matrix

$$W_{11;11} - W_{22;11} = W_{12;12} , \tag{A.23}$$

we can rewrite Eq. (A.22) into the following form:

$$\left\{-\sigma^2 I_{11} - 2\left(\Omega^2 I_{11} - W_{12;12}\right)\right\} (X_{11} - X22) - 2i\Omega I_{11} (X_{21} + X_{12}) = 0 . \tag{A.24}$$

Similarly, adding Eqs. (A.14) to (A.15), we have

$$\left\{-\sigma^2 I_{11} - 2\left(\Omega^2 I_{11} - W_{12;12}\right)\right\}(X_{12} + X21) + 2i\Omega I_{11}(X_{11} - X_{22}) = 0 \quad . \tag{A.25}$$

By combining Eqs. (A.24) and (A.25) into a matrix form, we finally obtain

$$\begin{pmatrix} -\sigma^2 I_{11} - 2\left(\Omega^2 I_{11} - W_{12;12}\right) & -2i\Omega I_{11} \\ 2i\Omega I_{11} & -\sigma^2 I_{11} - 2\left(\Omega^2 I_{11} - W_{12;12}\right) \end{pmatrix} \begin{pmatrix} X_{12} + X_{21} \\ X_{11} - X_{22} \end{pmatrix} = \begin{pmatrix} 0 \\ 0 \end{pmatrix} \tag{A.26}$$

For the existence of non-trivial solution to Eq. (A.26), the determinant of the matrix which appears in the left hand side of Eq. (A.26) must be equal to zero. Thus, we have

$$I_1 1^2 \sigma^4 - 4W_{12;12} I_{11} \sigma^2 + 4\left(\Omega^2 I_{11} - W_{12;12}\right)^2 = 0 \quad . \tag{A.27}$$

This fourth-order algebraic equation has roots which are written by

$$\sigma = \Omega \pm \frac{1}{I_{11}} \left\{I_{11}\left(2W_{12;12} - I_{11}\Omega^2\right)\right\}^{1/2} \tag{A.28}$$

and

$$\sigma = -\Omega \pm \frac{1}{I_{11}} \left\{I_{11}\left(2W_{12;12} - I_{11}\Omega^2\right)\right\}^{1/2} \quad . \tag{A.29}$$

When $W_{12;12}$ is equal to $I_{11}\Omega^2$, σ becomes zero and the equilibrium figure is neutral against such perturbations. Moreover, when 2 $W_{12;12}$ becomes less than $I_{11}\Omega^2$, σ becomes complex. Then, the amplitude of the perturbation increases with time and the equilibrium figure becomes unstable. Chandrasekhar and Lebovitz (1962) showed these relations coincide exactly with those which are known for the stability of the Maclaurin spheroid.

REFERENCES

Benz, W., Slattery, W. L., and Cameron, A. G. W. 1986. The Origin of the Moon and the Single Impact Hypothesis I. *Icarus* **66**, 515 - 535

Benz, W., Slattery, W. L., and Cameron, A. G. W. 1987. The Origin of the Moon and the Single Impact Hypothesis II. *Icarus* **71**, 30 - 45

Benz, W., Cameron, A. G. W., and Melosh, H. J. 1989. The Origin of the Moon and the Single Impact Hypothesis III. *Icarus* **81**, 113 - 131.

Boss, A. P. 1986 Protoearth Mass Shedding and the Origin of the Moon. *Icarus* **66**, 330-340.

Boss, A. P. and Mizuno, H. 1984. The dynamic fission instability and the origin of the Moon (Abstract). In *Papers Presented to the Conference on the Origin of the Moon*, p. 36, Lunar and Planetary Institute, Houston.

Boss, A. P. and Mizuno, H. 1985. Dynamic Fission Instability of Dissipative Protoplanets. *Icarus* **63**, 134.

Boss, A. P. and Peale, S. J. 1986. Dynamical Constraints on the Origin of the Moon. In *Origin of the Moon* (Houston: Lunar and Planetary Institute), pp. 59-101.

Burns, J. A. 1986. The Evolution of Satellite Orbits. In *Satellites* (Tucson: Univ. of Arizona Press), pp. 117-158,

Cameron, A. G. W. and Benz, W. 1991. The Origin of the Moon and the Single Impact Hypothesis IV. *Icarus* **92**, 204 - 216.

Chandrasekhar, S. 1961. *Hydrodynamic and Hydromagnetic Stability* . (New York: Dover Publications).

Chandrasekhar, S. 1969. *Ellipsoidal Figures of Equilibrium.* (New York: Dover Publications).

Chandrasekhar, S. and Lebovitz, N. R. 1962, On the Oscillations and the Stability of Rotating Gaseous Masses. *Ap. J.* **135**, 248-260.

Clayton, R. N., Onuma, N., and Mayeda, T. K. 1976. A Classification of Meteorites Based on Oxygen Isotopes. *Earth Planet. Sci. Lett.* **30**, 10-18.

Darwin, G. H. 1879. On the Precession of a Viscous Spheroid, and on the remote history of the Earth. *Philos. Trans. Roy. Soc.*, **170**, 447-530.

Darwin, G. H. 1880. On the secular changes in the elements of the orbit of a satellite revolving about a tidally distorted planet. *Philos. Trans. Roy. Soc.*, **171**, 713-891.

Drake, M. J. 1986. Is Lunar Bulk Material Similar to Earth's Mantle? In *Origin of the Moon* (Houston: Lunar and Planetary Institute), pp. 105-124.

Durisen, R. H. and Gingold, R. A. 1986. Numerical Simulations of Fission. In *Origin of the Moon* (Houston: Lunar and Planetary Institute), pp. 487-498.

Durisen, R. H. and Scott, E. H. 1984. Implications of recent numerical calculations for the fission theory of the origin of the Moon. *Icarus* **58**, 153-158.

Eriguchi, Y. and Hachisu, I. 1983. Two Kinds of Axially Symmetric Equilibrium Sequences of Self-Gravitating and Rotating Incompressible Fluid. *Progress of Theoretical Physics* **69**, 1131-1136.

Eriguchi, Y., Hachisu, I. and Sugimoto, D. 1982. Dumb-Bell-Shape Equilibria and Mass-Shedding Pear Shape of Selfgravitating Incompressible Fluid. *Progress of Theoretical Physics* **67**, 1068-1075.

Eriguchi, Y., Hachisu, I. 1985. Maclaurin Hamburger Sequence. *Astron. Astrophys.* **146**, 289-292.

Eriguchi, Y. and Müller, E. 1985. A General Computational Method for obtaining equilibria of self-gravitating and rotating gasses. *Astron. Astrophys.* **146**, 260-268.

Eriguchi, Y. and Sugimoto, D. 1981. Another Equilibrium Sequence of Self-Gravitating and Rotating Incompressible Fluid. *Progress of Theoretical Physics* **65**, 1870-1875.

Ferrari, A. J., Sinclair, W. S., Sjogren, W. L., Williams, J. G., and Yoder, C. F. 1980. Geophysical Parameters of the Earth-Moon System. *J. Geophys. Res.* **85**, 3939-3951.

Giuli, R. T. 1968. On the Rotation of the Earth Produced by the Gravitational Accresion of Particles. *Icarus* **8**, 301-323.

Harris, and Kaula, 1975. A co-accretional model of satellite formation. *Icarus* **24**, 516-524.

Hartmann, W. K. and Davis, D. R. 1975. Satellite-Sized Planetesimals and Lunar Origin *Icarus* **24**, 504 - 515

Hood, L. L. and Jones, J. 1985. Lunar Density Models Consistent with mantle seismic velocities and other geophysical constraints (abstract). In *Lunar and Planetary Science XVI*, (Houston: Lunar and Planetary Institute) pp. 360-361.

Ida, S. and Nakazawa, K. 1990. Did Rotation of the Protoplanets Originate from the Successive Collisions of Planetesimals? *Icarus* **86**, 561-573.

Ida, S. and Makino, J. 1993. Scattering of Planetesimals by a Protoplanet: Slowing Down of Runaway Growth. *Icarus* **106**, 210-227.

Jeffreys, H. 1930. Amplitude of Tidal Resonances. *Mon. Not. Roy. Astron. Soc.*, **107**, 260-272.

Kato, T. and Ringwood, A. E. 1989. Was the Moon Formed from the Mantle of a Martian-sized Planetesimal? *Lunar Planet. Sci* **20**, 510-511.

Lissauer, J. J. and Kary, D. M. 1991. The Origin of the Systematic Component of Planetary Rotation I. Planet on a Circular orbit. *Icarus* **94**, 126-159.

Mignard, F. 1982. Long time integration of the Moon's orbit. In *Tidal Friction and the Earth's Rotation II* (New York: Springer-Verlag), pp. 67-91.

Nakazawa, K., Komuro, T., and Hayashi, C. 1983. Origin of the Moon - Capture by Gas Drag of the Earth's Primordial Atmosphere. *The Moon and Planets* **28**, 311 - 327.

Ohtsuki and Ida, 1995. In preparation.

Okuchi, T. 1995. The Moon from the terrestrial magma ocean. Master Thesis, Tokyo Institute of Technology.

Rammensee, W. and Wänke, H. 1977. On the partition coefficient of tungsten between metal and its bearing on the origin of the Moon. *Proc. Lunar Sci. Conf. 8th*, 399-409.

Ringwood, A. E. 1960. Some Aspects of the Thermal Evolution of th Earth. *Geochim. Cosmochim. Acta* **20**, 241-259.

Ringwood, A. E. 1979. *Origin of the Earth and Moon.* (New York: Springer - Verlag).

Ringwood, A. E. 1989. The Earth-Moon Connection. *Z. Naturforsh* **44a**, 891-923.

Ringwood, A. E. and Kesson, S. E. 1977. Basaltic Magmatism and the Bulk Composition of the Moon, II. Siderophile and Volatile Elements in Moon, Earth and Chondrites: Implications for Lunar Origin. *The Moon* **16**, 425-464.

Ruskol, E. L. 1961. The origin of the Moon - I. *Soviet Astronomy - AJ*, **4**, 657-668.

Ruskol, E. L. 1963. The origin of the Moon - II. *Soviet Astronomy - AJ*, **7**, 221-227.

Tanaka, H. and Ida, S. 1995. Distribution of Planetesimals around a Protoplanet in the Nebula Gas: I. The semi-analytic calculation of the gravitational scattering by a protoplanet. submitted to *Icarus*

Tasssoul, J. L. 1978. *Theory of Rotating Stars.* (New Jersey: Princeton Univ. Press).

Tassoul, J. L. and Ostriker, J. P. 1968. On the Oscillations and Stability of Rotating Stellar Models. I. Mathematical Techniques. *Ap. J.* **154**, 613-626.

Taylor, S. R. 1986. The Origin of the Moon: Geochemical Considerations. In *Origin of the Moon* (Houston: Lunar and Planetary Institute), pp. 125-143,